Impact of Organics and Carbonates on the Oxidation and Precipitation of Iron during Hydraulic Fracturing of Shale

Adam D. Jew[1,2*], Megan K. Dustin[2], Anna L. Harrison[1,2], Claresta M. Joe-Wong[2], Dana L. Thomas[2], Katharine Maher[2], Gordon E. Brown, Jr.[1,2,3], and John R. Bargar[1]

1) *Stanford Synchrotron Radiation Lightsource, SLAC National Accelerator Laboratory, 2575 Sand Hill Rd., Menlo Park, CA 94025, USA*
2) *Department of Geological Sciences, School of Earth, Energy, and Environmental Sciences, Stanford University, Stanford, CA 94305-2115, USA*
3) *Department of Photon Science, SLAC National Accelerator Laboratory, Stanford University, 2575 Sand Hill Rd., Menlo Park, CA 94025, USA*

*Corresponding Author: adamjew@stanford.edu

For Submission to Energy & Fuels

Abstract:

Hydraulic fracturing of unconventional hydrocarbon reservoirs is critical to the United States energy portfolio; however, hydrocarbon production from newly fractured wells generally declines rapidly over the initial months of production. One possible reason for this decrease, especially over time scales of several months, is the mineralization and clogging of microfracture networks and pores proximal to propped fractures. One important but relatively unexplored class of reactions that could contribute to these problems is oxidation of Fe(II) derived from Fe(II)-bearing phases (primarily pyrite, siderite, and Fe(II) bound directly to organic matter) by the oxic fracture fluid and subsequent precipitation of Fe(III)-(oxy)hydroxides. The extent to which such reactions occur and their rates, mineral products, and physical locations within shale pore spaces are unknown. To develop a foundational understanding of potential impacts of shale iron chemistry on hydraulic stimulation, we reacted sand-sized (150-250 µm) and whole rock chips (cm-scale) of shales from four different formations (Marcellus Fm., New York; Barnett Fm., Central Texas; Eagle Ford Fm., Southern

Texas; and Green River Fm., Colorado) at 80°C with synthetic fracture fluid, with and without HCl. These four shales contain variable abundances of clays, carbonates, and total organic carbon (TOC). We monitored Fe concentration in solution and evaluated changes in Fe speciation in the solid phase using synchrotron-based techniques. Solution pH was the most important factor affecting the release of Fe into solution. For reactors with an initial solution pH of 2.0 and low carbonate content in the initial shale, the sand-sized shale showed an initial release of Fe into solution during the first 96 hours of reaction, followed by a plateau or significant drop in solution Fe concentration, indicating that mineral precipitation occurred. In contrast, in reactors with high pH buffering capacity, little to no Fe was detected in solution throughout the course of the experiments. In reactors that contained no added acid (initial pH = 7.1), there was no detectable Fe release into solution. The carbonate-poor whole rock samples showed a steady increase, then a plateau in Fe concentration during 3 weeks of reaction, indicating slower Fe release and subsequently slower Fe precipitation. Synchrotron-based x-ray fluorescence mapping coupled with x-ray absorption spectroscopy (both bulk and micro) showed that when solution pH was above 3.25, Fe(III)-bearing phases precipitated in the shale matrix. Initially, ferrihydrite precipitated on and in the shale, but as experimental time increased, the ferrihydrite transformed to either goethite (at pH 2.0) or hematite (pH > 6.5). Additionally, not all of the released Fe(II) was oxidized to Fe(III), resulting in precipitation of mixed-valence phases such as magnetite. Idealized systems containing synthetic fracture fluid and dissolved ferrous chloride but no shale showed that in reactors open to the atmosphere at low pH (< 3.0), Fe(II) oxidation is inhibited. Surprisingly, the addition of bitumen, which is often extracted by organic compounds in the fracture fluid, can override this inhibition of Fe(II) oxidation caused by low pH. Nonetheless, O_2 in the system is still the most important factor controlling Fe(II) oxidation. These results indicate that Fe redox cycling is an important and complex part of hydraulic fracturing and provide evidence that Fe(III)-bearing precipitates derived from oxidation of Fe(II)-bearing phases could negatively impact hydrocarbon production by inhibiting transport.

Introduction:

Hydraulic fracturing in the United States has seen a strong increase in both the number of new wells being drilled and the re-fracturing of oil/gas shales that were previously hydraulically fractured[1]. Although hydraulic fracturing is positively impacting the energy landscape of the United States, production drops significantly within several months of initial hydrocarbon production[2-8]. The majority of modeling efforts examining declines in production of gas have focused on changes to advective flow due to a reduction in the subsurface pressure gradients caused by extraction[8]. Modeling results are generally consistent with initial production data provided by field operators; however, the discrepancy between model predictions and observations increases over time[8]. One possible cause for the late-stage model discrepancy and decrease in hydrocarbon production in these systems is the precipitation of minerals that can occlude pores, pore throats, fractures, and piping used during the fracturing process. There is a substantial amount of reduced Fe in oil/gas shales, and precipitation of Fe-bearing phases is known to be problematic in hydraulic fracturing[9]. Various Fe-controlling agents are added to the fluids injected into the subsurface, including citric acid, ethylene glycol, acetic acid, thioglycolic acid, and sodium erythorbate[10]. Although these chemicals, coupled with corrosion inhibitors, have been shown in simplified laboratory studies to inhibit the release of Fe (corrosion inhibitor) and the precipitation of Fe(III)-(oxy)hydroxides (Fe-controlling agent), produced water from hydraulic fracturing commonly contains significant quantities of Fe (including suspended crystalline Fe-bearing phases) in solution, indicating that the Fe-controlling agents in the subsurface do not eliminate Fe release into solution[11-17]. Due to the small size of fractures and pores in the subsurface rocks (ranging from nm's to mm's in diameter), even a small amount of Fe(III)-bearing precipitate has the potential to have a large impact on permeability[18-25]. A detailed investigation of Fe cycling in hydraulically fractured shales is required to determine the extent to which precipitation of Fe(III)-bearing solids does indeed occur and the chemical controls that govern this process.

To address these needs, as well as to determine if Fe-controlling agents do inhibit the formation of Fe(III)-precipitates in oil/gas shale systems, experiments were conducted in which shales from four different shale formations were reacted with synthetic hydraulic fracture fluid. The four shales chosen for study [Marcellus (New York), Barnett (Central Texas), Eagle Ford (South Texas), and Green River (Colorado)] offer a wide range of differences in carbonate, clay, and organic contents as well as in kerogen types. The focus of the present study is to determine: (1) which chemical processes are primarily responsible for Fe release from the shales, (2) which factors contribute to Fe(II) oxidation, and (3) the identity and locations of Fe-bearing solid phases before and after reaction with synthetic hydraulic fracture fluid. A combination of wet chemical, x-ray diffraction (XRD), and synchrotron-based imaging and x-ray absorption spectroscopic techniques was used to determine changes in Fe speciation throughout the

experimental process and provided valuable insights about the potential role of Fe(III)-bearing precipitates in limiting hydrocarbon production from hydraulically fractured shale systems. In addition, the experimental results help identify possible areas in which improvements to the hydraulic fracturing process can be achieved. This paper is a companion to a paper that used the sand-sized shale experiments to explore the controls on mineral dissolution, not limited to Fe-phases, and the implications of mineral-fluid reaction on porosity changes and the release of heavy metal contaminants from shale systems (Harrison *et al*., *in press*). Here, we focus solely on the dynamics of Fe-cycling, and present additional experimental results that help us assess the role of organics on Fe-cycling.

These experiments were designed to examine chemical reactions that occur in shale pore space at the onset of fracture fluid-shale reactions, prior to and during neutralization of acid. The crucial time period for these reactions is between 1 and 10 days because most shale alteration occurs in this interval. Acid is generally injected into formations within a few hours, before acid neutralization can occur. Consequently acid-driven shale alteration is expected to be widespread within new stimulated fractures. The salinity of shale pore fluids during these early times is expected to be controlled by the composition of the injected fluid and the solid phases present and not by TDS present in flowback or produced water. Flowback does not occur until much later, when the well is unplugged, typically after several weeks. For this reason, our experiments cannot be compared directly to flowback water conditions.

Methods

Shale Samples:

Samples from the Marcellus shale (Oatka Creek Member, New York), Eagle Ford shale (South Texas), Barnett shale (Central Texas), and Green River shale (Mahogany Ledge Member, Colorado) were selected for experimentation due to their significant differences in clay, carbonate, and organic matter contents. Although there are significant variations in mineralogy in each of the different shales (*i.e.* Marcellus shale contains regions with high carbonate and low clay as well as regions with low carbonate and high clay), samples were selected in order to investigate a wide range of differing shale mineralogies. The Marcellus shale (GPS: Lat. 42.98, Long. -77.99) and Green River shale (GPS: Lat. 39.58, Long. -107.89) samples used were outcrop samples collected in July 2016 and August 2015, respectively. Barnett and Eagle Ford samples are core samples taken at depth (2613 m and 3915 m, respectively). Due to proprietary information involving the Eagle Ford and Barnett shale samples, their sample localities can not be divulged in this work.

Fracture-Fluid Composition:

The fracture fluid recipe used in these experiments (**Table 1**) is similar to that used in the National Energy Technology Laboratory's (NETL) Marcellus Well E in Greene County, PA[23]. Because the present study focuses on the release of Fe from shale, silica proppants were not included in the reactors. Additionally, due to the very low quantities of two biocides (2,2-dibromo-3-nitrilopropionamide and dibromoacetonitrile) compared to polyethylene glycol, the additional biocides were not used in our fracture fluid formulation. After a comparison between the chemical recipe used by NETL and other recipes employed in the Marcellus region, using the FracFocus online database[10], we chose the recipe outlined in **Table 1** as a reasonable approximation of fracture fluid for this region. Though not every hydraulic fracturing operation uses HCl, either for well bore cleaning or throughout the injection process, it is used in a significant proportion of operations (> 55% nationwide and nearly 100% in carbonate-rich shales)[10]. The largest difference between the composition of this fluid and those used in the Texas region (Eagle Ford and Barnett) is the replacement of ethylene glycol used in cold weather regions, such as the Marcellus Shale, with methanol as the main solution corrosion inhibitor. Because methanol and ethylene glycol are generally considered to have similar binding affinities for iron, using the Marcellus fracture fluid for Eagle Ford and Barnett samples is not expected to change the reaction mechanism and reaction products in a significant way. In an industrial setting, different chemicals are injected at different times over a 12-hour period and in general are left for a period of 3 weeks prior to extraction. Given the long time frame of the experiments, the impracticality in doing multiple chemical injections, and the strong likelihood of mixing in the subsurface, all chemicals for the fracture fluid were mixed together prior to addition to reactors and introduced to the shale samples all at once. The final pH of the solution with all chemicals added, including HCl, was pH = 2.0.

Bitumen Extraction:

Chemicals common to almost all fracture fluids[4] have the ability to extract bitumen from oil/gas shales in the field, with dibromoacetonitrile and 2-ethyl hexanol being the dominant extractants[26, 27]. Use of these additives will therefore result in liberation of bitumen within the shale pores and fracture space, with the possibility of subsequent reaction with Fe. To study the impact of bitumen on iron cycling dynamics, bitumen was extracted from Marcellus and Green River shale samples for use in idealized Fe systems described later by following the first two extraction steps outlined by Göklen *et al*., which were designed to extract kerogen from the Green River Shale[28]. The first step consists of reaction of the shale with a 3N hydrochloric acid (HCl) solution at 70^{o}C to remove carbonates. The second step, designed to remove bitumen, utilizes a Soxhlet extractor charged with 3:1 toluene to methanol. After bitumen was extracted, the toluene/methanol solution containing bitumen was placed in a desiccator connected to a vacuum pump that vented into a fume hood to remove the high vapor pressure toluene and methanol and leave behind the bitumen for use in our bitumen/Fe experiments.

Shale/Fracture Fluid Reactors:

Experiments consisted of 3-week, 3-month, and 6-month long reactions performed in 250 mL glass bottles with butyl-rubber stoppers that were partially permeable to O_2. Experiments were also conducted with an Ar-filled headspace (125 mL bottles) with thicker butyl-rubber stoppers to eliminate O_2 intrusion. All glassware was acid washed, triple rinsed in double deionized (DDI) water (18.2 MΩ), and heated in a furnace overnight at 700^{O}C. To remove any leachable organics from the butyl-rubber stoppers, both types of stoppers were immersed in boiling 0.1 M KOH for one hour and then triple rinsed in DDI water prior to use.

The 250 mL reactors were filled with 1 g of shale material, either sand-sized particles (250-350 μm) or shale chips (0.5-1 cm), and 200 mL of fluid, resulting in 50 mL of headspace. The shale material consisted of Marcellus, Eagle Ford, Barnett, or Green River samples. Additionally, corundum (α-Al_2O_3) chips were added to reactors to act as substrates for secondary mineral precipitation. The fluid compositions added to reactors were varied as follows: (1) synthetic fracture fluid with added HCl; (2) fracture fluid with no HCl; (3) DDI water only; and (4) HCl only. The solutions and headspace were not sparged with inert gas, resulting in solutions and headspaces that were initially at equilibrium with the atmospheric gases at 20˚C. Injected fluids in hydraulic fracturing operations are often at equilibrium with the atmosphere making the unsparged reactors with Ar headspace the closest analog to real-world systems. Though the unsparged reactors with air as headspace contains slightly elevated O_2 concentrations compared to real-world systems, the end result would be a slight increase in the amount of Fe(II) oxidation versus the Ar headspace reactors. Dissolved oxygen in produced waters is high (5-10 mg/L dissolved O_2)[29]. Sealed reactors were incubated in a convection oven at 80^{o}C.

The smaller 125 mL bottles had the same solid/liquid/headspace ratio as in the 250 mL reactor bottles (0.5 g shale, 100 mL fluid, and 25 mL headspace). Because these smaller reactors were used to investigate the effect of O_2 in the fluid and headspace, the fluid and/or the headspace were purged with ultra-high purity Ar. Sealed reactors were incubated in a convection oven at 80^{o}C.

Bitumen/Fe Oxidation Experiments:

The main goal of these experiments was to determine the following: (1) if Fe(II) oxidation occurs in shales under various pH conditions, (2) if any fracture fluid components could enhance aqueous Fe(II) oxidation, and (3) if bitumen enhances aqueous Fe(II) oxidation. Experimental reactors containing 40 ppm dissolved Fe(II) in the form of $FeCl_2$ were used to determine the effect of fracture fluid, pH, O_2, and bitumen on the oxidation of Fe(II).

Fracture fluid was synthesized without HCl. To minimize the possibility of photo-induced oxidation of Fe(II) in the reactors, all reactors were wrapped in Al foil prior to the addition of any solution. For samples open to the atmosphere, 250 mL bottles were filled with 200 mL of solution so that aqueous samples could be taken throughout the experiment while leaving enough potential Fe(III)-containing precipitate in the bottle for later XRD analysis. For reactors containing added bitumen (derived from Marcellus or Green River), the total concentration of bitumen was set at 40 ppm. The bitumen concentration selected for these reactors is the average of the theoretical bitumen concentrations released from Marcellus and Green River shales based on the solubility of bitumen in 2-ethyl-1-hexanol[27], and the total amount of bitumen contained in the rock samples. Additionally, 40 ppm bitumen provided a 1:1 Fe:Bitumen molar concentration which is a reasonable ratio for the Marcellus shale. Though pH should have little to no effect on bitumen solubility[27, 30, 31], the initial pH for the reactors was set at either 2.0 or 7.1 to determine the effect of pH on Fe(II) oxidation in the presence of bitumen. For reactors with excess O_2, the fluid was allowed to freely exchange with the laboratory atmosphere. For de-oxygenated reactors, a total of 100 serum bottles (20 mL capacity) containing 10 mL of solution were prepared. Samples were incubated at 80^{o}C and sacrificed at 0, 2, 5, 8, 17, 24, and 48 hours. In order to limit any addition of O_2 into Ar-sparged reactors, sampling via needle and syringe of serum bottles was limited to one time only. After all components were added to the serum bottles and de-oxygenated (if necessary), a de-oxygenated solution of $FeCl_2$ was added to the vials via syringe to reach a final aqueous Fe(II) concentration of 40 ppm. The cleaning procedure for the serum bottles was the same as described earlier. In the de-oxygenated reactors the fracture fluid and serum bottles were sparged with ultra high purity Ar. Sampling and Fe analysis of the samples are described below.

pH and Fe Sampling and Analysis:

Reactor experiments lasting a total of 3 weeks were sampled at 0, 6, 12, 24, 48, 96, 192, 384, and 504 hours. The 3-month reactors were sampled every 10 days for a total of 90 days, while the 6-month reactors were sampled every 20 days over a total period of 180 days.

At each time point, 5 mL of solution was taken from each reactor via needle and syringe with minimal agitation to the reactor bottles. The solution was filtered through a 0.2 μm polyethersulfone (PES) syringe filter into a 15 mL polypropylene centrifuge tube. Following sampling, the butyl-rubber stoppers were sealed with silicone to minimize gas leakage through areas of the stopper that the needle punctured, and the bottles were returned to the oven. Measurements of pH, Fe(II) concentration, and total Fe concentration were carried out immediately following sampling and filtration. Iron(II) and total iron concentrations were determined using Ferrozine and hydroxylamine hydrochloride, respectively, with absorbance

being measured using a Hewlett-Packard model 8452 photo diode array UV/Vis spectrophotometer at a wavelength of 562 nm.

Bulk XRF Measurements:

Total elemental compositions of the shale were measured using x-ray fluorescence (XRF) analysis in the Stanford Environmental Measurements Laboratory. The shale samples were analyzed using a Spectro Analytical XRF model XEPOS HE. A standard reference material, NIST SRM 2710a (Montana soil), was analyzed in addition to our shale samples to confirm the accuracy of the technique.

FIB-SEM Imaging:

Pyrite framboids in the Marcellus shale were imaged at the Stanford Nano Shared Facility using a FEI Strata 235DB DualBeam Focused Ion Beam-Scanning electron microscope (FIB-SEM) with an operating voltage of 5.0 kV.

Dynamic Light Scattering Measurements:

The particle size of the bitumen extracted from the Marcellus shale was measured using a Malvern Zetasizer model Nano-ZS. Bitumen was suspended in DDI water and measured in a quartz cuvette for a total of 40 scans.

X-ray Diffraction Measurements:

Bulk mineralogy of the shale samples and idealized Fe reactors was determined by x-ray diffraction (XRD). Powdered samples were analyzed on a Rigaku model CM2029 powder x-ray diffractometer using a Cu Kα x-ray source over a 2θ range of 5-70^{o}, and data were analyzed using the JADE diffraction software package[32]. Peak identification was accomplished by matching the four most intense diffraction peaks for a given mineral to diffraction patterns in the National Institute of Standards and Technology (NIST) database. In addition to mineral identification, the JADE software was used for quantitative analysis of the different phases by least squares fitting of the data; NIST diffraction patterns of reference compounds were used to fit the diffraction patterns of the samples.

Synchrotron-Based X-ray Spectroscopy and X-ray Fluorescence Imaging:

Unreacted and reacted samples of Barnett, Marcellus, Eagle Ford, and Green River shales were analyzed using synchrotron-based micro-x-ray fluorescence (μ–XRF) mapping and μ-X-ray Absorption Near Edge Structure (μ–XANES) spectroscopy on beamline 2-3 at the Stanford Synchrotron Radiation Lightsource (SSRL). Beamline 2-3 consists of a bending magnet insertion device using two water-cooled Si(111) monochromator crystals in the Φ = 90^{o} orientation to

select x-ray energy. Both μ-XRF maps and μ-XANES spectroscopy data were collected using a three-element vortex detector in fluorescence mode. The beam energy was set to 15 keV with a 2 μm x 2 μm beam size. The detection limit was approximately 50 ppm per pixel for each elemental map collected. Regions with high Fe content were chosen for Fe μ-XANES data collection. Iron K-edge μ-XANES spectra were collected from 250 eV below to 400 eV above the Fe K-edge (7112 eV). Energy calibration was done using an Fe metal foil placed behind the I_1 ion chamber. Multiple energy maps at 7122, 7128, and 7133eV were collected to determine the spatial distribution of Fe(II) versus Fe(III). Descriptions of data analysis for μ-XRF and μ-XANES data are given in the next subsection.

Bulk fluorescence yield Fe K-edge EXAFS spectra for the shale samples were collected on SSRL beamline 4-1, which has a wiggler insertion device and uses two water-cooled Si(220) monochromator crystals in the $\Phi = 0^{o}$ orientation. Extended X-ray Absorption Fine Structure (EXAFS) data were collected in fluorescence yield mode using a passivated implanted planar silicon detector. An Fe-metal foil was inserted between the second and third ion chambers for continuous energy calibration. Samples were maintained at 77K using a LN_2 cryostat during EXAFS data collection to reduce thermal disorder and make second-neighbor atoms easier to detect. Three scans were collected for all samples with a maximum *k*-range of 15 $Å^{-1}$.

X-ray Absorption Spectroscopy and X-ray Fluorescence Imaging Analysis:

The μ-XRF maps were processed and analyzed using the SMAK[33] software package, whereas bulk EXAFS and μ-XANES spectra were analyzed using the SixPACK[34, 35] software package. Both μ-XANES and EXAFS spectra were fit by linear combination fitting (LCF) using previously collected x-ray absorption spectra (XAS) of various Fe-bearing compounds. μ-XANES data were fit from 100 eV below to 350 eV above the Fe K-edge. Due to issues with glitches in the EXAFS data, the EXAFS data were fit from $k = 3$ to $k = 12$ $Å^{-1}$. Goodness-of-fit was determined by calculating the residual of the fit using one-component or multi-component fits and the following formula, where ν represents the $k^3\chi(k)$ value of the EXAFS data:

$$\text{Residual} = \frac{\sum_{t=1}^{n} (\nu_{data} - \nu_{fit})^2}{n}$$

Shell-by-shell fitting of the data was used to identify an oscillation in the EXAFS data that could not be fit with inorganic Fe reference compounds currently in our spectrographic reference library. More than 30 single-scattering pathways for Fe-O, Fe-C, Fe-S, Fe-B, Fe-N, Fe-CN, Fe-NO_3, Fe-SO_3, and Fe-SO_4 of varying backscatterer distances were created using literature data

for typical Fe(II)-X distances in organo-metallic molecules[36] and the single-scattering pathway generation module in the SixPACK software package using FEFF 6L[34, 35, 37].

Results:

Impact of Fracture Fluid on Shale Mineralogy - The four shales used in this work had large variations in clay, carbonate, pyrite, and organic contents. The Barnett shale contains the highest clay content (40.6 wt.%) of the four shales, followed by Marcellus, Oatka Creek, (35.0 wt.%), Eagle Ford (7.6 wt.%), and Green River, Mahogany Ledge (<1 wt.%) (**Table 2**). By definition, the Green River Shale samples used are not true shales because of the lack of significant quantities of clays; however, we will continue to use the term Green River Shale due to the historical use of this term for the Green River formation. As seen in **Table 2**, the Barnett, Marcellus, and Green River shales have illite as the dominant clay mineral. The dominant clay mineral in the Eagle Ford shale is kaolinite. Carbonate mineralogy (**Table 2**), which is a good indicator of the pH buffering capacity of a rock, differs significantly among the shale samples, with Eagle Ford having the highest carbonate content (64.5 wt.%), followed by Green River (54.6 wt.%), Marcellus (12.7 wt.%), and Barnett (8.2 wt.%). Calcite is the dominant carbonate mineral found in the Marcellus, Eagle Ford, and Barnett samples (> 80%), with minor amounts of dolomite. The Green River shale contains significant dolomite (28.9 wt.%) as well as calcite (23.2 wt.%) (**Table 2**).

Quantitative XRD results (**Table 2**) show a high consistency between duplicate samples along with distinct trends in mineralogy with reaction time. Throughout the reaction of the Marcellus samples, pH rose from the initial pH = 2.0 (**Figure 1**) to pH = 3.4. Neutralization of the acidic fracture fluid is reflected in the lack of detectable carbonate minerals post-reaction (**Table 2**). Throughout the reaction time there was a significant increase in the illite content from an initial concentration of 35.0 wt.% to 43.8 wt.% at the end of 6 months. During the same time period, the concentration of pyrite decreased from an initial value of 6.4 wt.% to a final value of 4.2 wt.%, indicating significant pyrite dissolution and release of Fe(II) into solution. Barnett samples showed the least amount of alteration throughout the entire 6-month experimental period as indicated by both the lack of change in mineralogy (**Table 2**) and the lack of any significant neutralization of the acidic solution (**Figure 1**). Unlike the Marcellus and Barnett samples where all the carbonate was lost during reaction, the Eagle Ford and Green River samples still contained significant quantities of carbonates even after 6 months of reaction. As indicated by pH measurements (**Figure 1**), reaction of the fracture fluid with the shale caused the pH of the fracture fluid to increase from 2.0 to > 6.0 within the first 48 hours of reaction and then the pH stabilized for the remainder of the experimental time. The concentration of carbonate minerals remaining in both the Eagle Ford and Green River samples was still > 50 wt.% following reaction in all experiments. In the case of the Green River shale,

calcite was preferentially dissolved relative to dolomite. Comparison of quantitative XRD results before and after 3 weeks of reaction of the shale samples often shows an increase in the overall concentrations of quartz and pyrite. This increase is due to re-normalization of the remaining phases following the removal of significant quantities of carbonate minerals from the shale samples because of dissolution (**Table 2**). Similar to the Marcellus shale, there is a detectable decrease in pyrite concentration in the Eagle Ford sample from 4 wt.% after 3 weeks of reaction time to 2.8 wt.% after the 6 months of reaction time. Although pyrite was not detectable by XRD in the Green River samples, there is abundant pyrrhotite in these samples as shown by synchrotron XRF mapping coupled with μ-XANES and bulk EXAFS spectroscopy as discussed below.

Changes in Bulk Sample Composition - A list of major and selected trace elements in the shales before and after reaction with fracture fluid is presented in **Table 3**. Total iron in the solid samples for Marcellus and Barnett shales dropped significantly with reaction time (**Table 3**). Marcellus shale had an initial Fe concentration of 45.63 mg/g that dropped by ~5 mg/g or more throughout the course of reaction. Similar to the Marcellus shale experiments, the Barnett shale experiments also showed a loss of Fe from the solid samples from an initial concentration of 24.8 mg/g to less than 21.8 mg/g for all incubation times. Eagle Ford and Green River shales show no consistent trend for Fe concentrations with time. In the reactors for all four shales, there was a drop in total Ca in the solid material due to calcite dissolution. Total Ca concentrations in the Barnett and Marcellus shale reactors both decrease from initial concentrations of 4.2 wt.% (Marcellus) and 2.5 wt.% (Barnett) to below 0.2 wt.% by 3 months (**Table 3**). Although the Eagle Ford and Green River shales did show a decrease in total Ca concentrations at the end of 6 months of reaction, both shales still contained over 9 wt.% Ca. Of all the shale types, the Barnett shale was the only one that showed a significant reduction in carbon throughout the course of the experiments. This initial concentration of C in the unreacted shale was 16 wt.% and decreased to below 5 wt.% upon reaction with the fracture fluid. For all four shale types, Na and K showed little to no change throughout the experiments. Although there is variability in Al and Si in the reactors, because the shale samples were reacted in borosilicate glass containers with a corundum chip, it is difficult to ascertain if variations in elemental concentration are derived from changes in the shale or from the reaction vessel/corundum chip.

Evolution of Solution Composition - The carbonate content of the unreacted shale samples is the primary control on the pH of the shale-fracture fluid systems with time (**Table 2 and Figure 1**). In reactor experiments that included HCl, the starting pH was 2.0, but as reaction time increased, the pH in the Eagle Ford and Green River shale reactors increased to > 6.0, whereas the pH for the Barnett and Marcellus shale reactors rose only to 3 to 4. In all reactors that contained no HCl (3-week, 3-month, and 6-month), little to no Fe was released into solution as

shown in **Figure 2** for the sand-sized Marcellus samples. In reactors containing fracture fluid and HCl, Marcellus and Barnett shale samples showed a significant increase in Fe released into solution, followed by a decrease, suggesting precipitation of one or more Fe-bearing phases or sorption of Fe onto another solid. Under all experimental conditions examined for the Marcellus and Barnett shales, the Fe(II) and Fe_{tot} concentrations follow the same trends, with Fe_{tot} being slightly higher in concentration, indicating the presence of dissolved or colloidal Fe(III). In the case of the Eagle Ford and Green River shale samples, which contain > 50 wt.% carbonates, there was little to no detectable Fe in solution (**Figure 2**). The Fe solution data for Marcellus and Barnett whole shale chips show a highly retarded Fe release when compared with the sand-sized particles due to the lower surface area per unit mass of the large chips. Both the Eagle Ford and Green River whole shale chip reactors had no detectable Fe in solution, which is similar to our findings for the sand-sized Eagle Ford and Green River samples.

Iron Mineralogy Evolution at the Micron Scale – Micro-XRF mapping and Fe K-edge μ-XANES spectroscopy were conducted in order to image Fe distribution and determine Fe speciation on micron scales on single sand-sized shale grains. This approach is preferred rather than using bulk XAS techniques, which provide speciation information averaged over hundreds of sand-sized particles. The x-ray beam for μ-XRF imaging penetrates over 30 μm into the sample, providing imaging and speciation information for the surface of particles as well as into the shale matrix. The Fe(II) and Fe(III) maps of the unreacted samples for all four shales are shown in **Figure 3**. Multiple-energy XRF mapping of the unreacted sand-sized shale samples of all four shale types below and above the Fe K-edge shows minor amounts of Fe(III)-bearing phases around the margins of Fe(II)-bearing particles in the samples. μ-XANES analysis of Fe(II) hot spots in the Barnett, Marcellus, and Eagle Ford shales shows that they are pyrite (**Figure 3**). Scanning electron microscopy (SEM) shows that these grains have a dominantly framboidal texture, consistent with pyrite morphology (**Figure 4**). Although the particles such as in **Figure 3** are exclusively pyrite in the Barnett, Marcellus, and Eagle Ford shales, other pyrite framboids examined in these samples often contained a mixture of pyrite and magnetite. In contrast, μ-XANES analysis of the Fe(II) hot spots in the Green River shale shows that the primary Fe(II)-sulfide is pyrrhotite rather than pyrite. Additionally, analyses of the μ-XANES spectra of Fe-rich particles in the Green River samples indicate Fe(III) in goethite, ilmenite, potassium feldspar, as well as trace amounts of hematite.

The pyrite content of the shales, which ranges from 2.1 to 6.4 wt.% (**Table 2**), is the largest source of inorganic Fe and is therefore one of the most important variables with regard to iron cycling in these shales. Based on XRD and XRF results (**Tables 2 and 3**), pyrite in these samples comprises ≥ 90% of the total initial inorganic Fe pool, with additional iron from siderite and clays; however, XRF mapping and μ-XANES spectroscopy also showed the presence of magnetite in all four shales. In addition, pyrrhothite is the only iron sulfide detected in the

Green River samples. In all of the unreacted shale samples investigated, regardless of whether the samples are outcrop or core samples, some Fe(III) is present as shown in **Figure 3**. μ-XANES analyses of the Fe(III)-rich areas indicate that the main Fe(III)-bearing phase present in all four sample types is magnetite, although Fe(II) is still the dominant form of iron in the unreacted shales.

Following reaction with fracture fluid, a significant amount of Fe in Marcellus shale (**Figure 5**) and Eagle Ford shale (**Figure 6**) is redistributed as Fe(III)-bearing precipitates. This finding indicates that Fe(II) released from the pyrite as a result of reaction with the acidic fracture fluid was oxidized and precipitated as Fe(III)- and Fe(II/III)-bearing phases. Although Fe(III)-bearing precipitates are spatially associated with Fe(II) hot spots in the Green River and Eagle Ford samples (**Figures 5 and 6**), Fe(III) in the Marcellus and Barnett samples (data not shown) is diffuse and spread out over the particle. In the case of the Eagle Ford and Green River samples, Fe(III) occurs in discrete zones that are tens of microns in diameter. μ-XANES spectra were collected at numerous locations for all four shale samples, and the results for the Marcellus and Eagle Ford shales are presented below.

Because of the economic importance and significant differences between the Marcellus and Eagle Ford shales, we focused our μ-XANES study on these two samples. For both, μ-XANES spectra were collected around pyrite grains, which revealed varying concentrations of Fe(II) and Fe(III) (**Figures 5 and 6**). The Marcellus sample contains distinct regions that are Fe(II) rich (**Figure 5A**). As illustrated in **Figure 5C**, there is a significant change in the shape of the μ-XANES spectra as the proportion of Fe(II) to Fe(III) changes. The XANES spectra of numerous Fe(II)-, Fe(II/III)-, and Fe(III)-bearing phases were used in the linear combination fitting of these μ-XANES spectra as seen in **Figures 5C and 5D**. In the Marcellus sample, the location (Spot 1) with the highest Fe(II) concentration was found to be predominantly pyrite (86%), with minor amounts of magnetite (14%) (**Figures 5A and 5D**). As Fe(II) concentrations decrease and Fe(III) concentrations increase, ferrihydrite and goethite were detected (**Figures 5B and 5D**). Magnetite was detectable in all four spots analyzed, indicating that not all of the Fe released from the pyrite framboids was fully oxidized prior to precipitation. Although magnetite was detected in unreacted samples, the amount and distribution differ from those of the reacted samples. In the unreacted samples the magnetite is lower in concentration and closely associated with the edges of pyrite grains. In contrast, in reacted samples the magnetite is intermixed with the pyrite grains (**Figures 5 and 6**) or hematite (**Figure 6**). The association of magnetite with the Fe(III)-oxides and pyrite was not seen in any of the unreacted samples. Reacted Eagle Ford shale samples showed even more pronounced Fe(III) mineral production, with the presence of large crystals (20-90 μm in diameter) that were not detectable in the unreacted shale (**Figures 6A and 6B**). As seen in **Figures 6A and 6B**, a new Fe(III)-dominant mineral grain formed due to exposure to the fracture fluid that is larger than the neighboring

pyrite framboid. The fits of the four μ-XANES spectra collected for the Eagle Ford sample are consistent with an array of Fe-bearing species. A fit of the μ-XANES spectra collected from the pyrite grain seen in Spot 4 (**Figure 6A**) suggests preferential removal of sulfur from the pyrite as indicated by the presence of pyrrhotite. Similar to the Marcellus samples, pyrite-rich zones in the Eagle Ford samples also tend to contain magnetite. Unlike the Marcellus sample, however, the Fe(III)-rich region seen in the Eagle Ford sample (**Figure 6B)** is dominated by hematite, whereas the Marcellus samples contain ferrihydrite and goethite, but not hematite.

The Barnett shale showed the least amount of pyrite alteration and the lowest concentrations of Fe(III)-bearing phases out of the four shale samples examined. The lack of significant Fe(III)-bearing phases is consistent with the minimal buffering of the low-pH fracture fluid (**Figure 1**) and little to no change in pyrite concentration shown by quantitative XRD (**Table 2**). Analysis of the μ-XANES spectra indicates that the Fe(III)-bearing regions in the reacted shale are comprised of magnetite, which may have been present in the rock before reaction, given that Fe(III) in the form of magnetite is detected in unreacted shale and does not appear to have been produced during the experiments (**Figure 3**).

The μ-XANES analysis of the Green River shale, following reaction, showed significant changes in Fe speciation. A total of five Fe-rich regions were selected for collection of μ-XANES spectra. Surprisingly, the five spectra collected were identical in shape. Differences among the μ-XANES spectra collected for the samples reacted for 3-weeks, 3-months, and 6-months were minimal, indicating little additional reaction of the Fe in the shale after three weeks. Because of the higher sensitivity of EXAFS spectra than XANES spectra to Fe speciation, the bulk EXAFS spectra of the reacted Green River shale are discussed below.

Impact of Fracture Fluid on Speciation of Iron in Bulk Shale - The bulk Fe K-edge EXAFS spectra are complex, with pyrite being the dominant Fe-bearing phase for the Marcellus, Barnett, and Eagle Ford shales we examined (**Table 4**). EXAFS analysis shows that the inorganic Fe species in the unreacted sand-sized samples of Marcellus, Barnett, and Eagle Ford shales include pyrite, goethite, ferrihydrite, and siderite (Eagle Ford only) (**Table 4**). As illustrated by the Marcellus shale (**Figure 7**), the most notable difference common to the Fe K-edge EXAFS spectra of all four shales samples is an additional oscillation in the spectra at k = 3.6 to 4.3 $Å^{-1}$ that is not found in the Fe K-edge EXAFS spectrum of any of the 30 inorganic Fe(II)- and Fe(III)-bearing reference compounds in our Fe XAS reference library. Because of this, shell-by-shell fitting of the spectra was necessary to determine the potential backscatterer causing this oscillation in the EXAFS spectra of the shale samples. The Fe K-edge EXAFS spectrum of an unreacted Marcellus shale sample was selected for the initial shell-by-shell fitting because this extra oscillation is particularly strong for the Marcellus shale. Over thirty FEFF-generated scattering pathways were created between Fe(II) or Fe(III) and the ligands S, O, N, B, C, NO_3, SO_3, SO_4, and CN at

distances reported for Fe organo-metallic molecules[36]. The shell-by-shell fitting indicates that S (organic), O, N, B, NO_3, SO_3, SO_4, and CN are not backscatterering ligands around Fe in the Marcellus shale sample. Instead, fitting of the EXAFS spectrum of the unreacted Marcellus shale indicates that C is the most likely ligand around Fe, with an Fe(II)-C bond distance of 2.11 ± 0.02 Å. Thus, the Fe-C single scattering pathway is responsible for the unexplained EXAFS oscillation at k = 3.6 to 4.3 $Å^{-1}$. This distance is consistent with literature data where the vast majority of Fe(II)-C bonds in organo-metallic molecules have bond distances between 2.06 and 2.14 Å[36]. The Fe(II)-organic phase is most likely associated with the kerogen present in the sample as blebs and ribbons dispersed throughout the shale (**Figure 8**). To get quantitative estimates of the proportion of the Fe-C pair correlation relative to Fe-inorganic species pair correlations in the shale samples, Fe-humate and ferrocene reference compounds were used in the linear combination fitting of the XANES spectra. The shell-by-shell fitting of the EXAFS spectra of the Fe-humate and ferrocene reference compounds shows that Fe is indeed bonded to the C in both reference samples with Fe-C distances of 2.08 ± 0.01 Å and 2.04 ± 0.02 Å, respectively. Once the Fe-humate (denoted as Fe-organic) was included in the LCF, fitting of the data improved significantly. In all unreacted and reacted shale samples, except for the unreacted Eagle Ford shale sample, the Fe-organic phase is detectable. The Fe-organic phase comprises between 12 and 33% of the total Fe species present in the shale samples (**Table 4**).

Similar to the results from μ-XANES analysis of the Green River shale, no pyrite was detected by bulk EXAFS analysis of this shale. Unlike the other shale samples, a significant portion of the Fe in the Green River shale is in the organic fraction. A shell-by-shell fit of the Fe K-edge EXAFS spectrum of the 3-week-reacted Green River shale (**Figure 9**) shows that the Fe-C scattering pathway makes a dominant contribution to the EXAFS spectrum, with an Fe-C distance of 2.13 ± 0.01 Å. The full EXAFS spectrum was fit using the Fe-C scattering pathway, along with the Fe-S (second-neighbor) and the Fe-Fe pathways from pyrite/pyrrhotite (**Figure 9**). The Fe-S first-neighbor pathway makes a relatively minor contribution and is difficult to resolve due to the very strong contribution of the Fe-C scattering pathway to the spectrum. Because of the complexity of the Green River EXAFS spectrum and the high variability in local structure of Fe bound to organic carbon, identifying the proper Fe-C organic reference compound for LCF analysis is challenging. However, by using the Fe K-edge EXAFS spectrum for the unreacted Green River shale and the spectrum for the 3-week reacted Green River kerogen isolated from the same shale material, useful information can be derived from LCF analysis. The 3-week-reacted Green River kerogen was selected for LCF because there is a detectable difference between the unreacted and 3-week-reacted kerogen in the Fe EXAFS data with a slight shift of the frequency of the EXAFS indicating a slightly shorter Fe-C bond distance (data not shown). There is no detectable difference between the 3-week- and 3-month-reacted kerogen samples (data not shown). By using the Fe K-edge EXAFS spectrum of the 3-week-reacted kerogen, a

more accurate fitting of the EXAFS spectrum of the 3-week-reacted shale could be accomplished (**Table 4**). The best fit of the EXAFS spectrum of the 3-week-reacted Green River shale is consistent with a combination of 55% of the unreacted shale and 45% of the 3-week-reacted kerogen. The ratio of shale to kerogen decreased significantly for the 3-month-reacted sample, with the unreacted shale component representing 40% and the isolated kerogen comprising 60% of the spectrum. There is virtually no difference between the 3-month- and 6-month-reacted samples.

Bitumen/Fe Interactions – The bitumens extracted from the Marcellus and Green River shales are physically and chemically very different. The bitumen extracted from the Marcellus shale was found to be mostly hydrophilic and readily dissolved into solution, whereas the Green River bitumen has the consistency of hard tar and is very hydrophobic. Marcellus-derived bitumen was the only bitumen that could be adequately dispersed into solution for dynamic light scattering analysis. The Marcellus bitumen has a bi-modal distribution of particle sizes, with one group of particles averaging 42 ± 3 nm in diameter and another group averaging 395 ± 15 nm in diameter.

The simplified reactors containing only Fe(II), as $FeCl_2$, and fracture fluid at pH = 2.0 (no bitumen) had no detectable Fe(II) oxidation during a 6-week incubation. The amount of Fe(II) oxidized was calculated by the loss of Fe(II) in solution compared with initial concentrations. Reactors with added bitumen had significant Fe(II) oxidation over a 48 hour incubation time for both pH 2.0 and 7.1 (**Figure 10**). The circum-neutral pH reactors with no fracture fluid showed the greatest Fe(II) oxidation, with Green River and Marcellus bitumen having 41% and 28%, respectively, of the Fe(II) oxidized to Fe(III) (**Figure 10**). The reactors containing fracture fluid, including an Fe controlling agent (ethylene glycol), showed a slightly lower amount of oxidized iron, with 25% oxidized for the Green River bitumen reactor and 23% oxidized for the Marcellus bitumen reactor. Iron(II) oxidation did occur in the reactor containing only circum-neutral pH fracture fluid (no bitumen), but the amount of oxidation was lower than in the bitumen-bearing circum-neutral pH reactors. At low pH the addition of bitumen resulted in enhanced oxidation of Fe in all reactors as well, but at lower amounts than at near-neutral pH, which is consistent with known pH effects on aqueous iron oxidation[38]. The presence of fracture fluid with bitumen at low pH dramatically enhanced Fe oxidation in both the Green River bitumen reactors (10% oxidized with no fracture fluid versus 20% oxidized with fracture fluid) and Marcellus bitumen reactors (6.5% oxidized with no fracture fluid versus 21.0% oxidized with fracture fluid) (**Figure 10**). XRD analysis of the Fe(III)-bearing precipitates indicates the presence of 2-line ferrihydrite in all the reactors in which Fe(III) precipitation occurred after 48 hours of incubation. When the reactors were allowed to incubate for 3 weeks, the 2-line ferrihydrite converted to goethite in reactors at pH = 2.0, whereas the 2-line ferrihydrite converted to hematite in the reactors at pH = 7.1. Idealized reactors with the oxygen removed

from the system did not show any Fe(II) oxidation regardless of the pH and the presence or absence of bitumen.

Discussion:

The reactivity of Fe-bearing species when exposed to fracture fluid varies significantly, depending on the mineralogy of the host shale. The Fe μ-XRF maps coupled with μ-XANES spectroscopy of the unreacted Barnett (2613 m depth), Marcellus (outcrop), Eagle Ford (3915 m depth), and Green River (outcrop) shales show that all samples exhibit common initial Fe speciation with Fe-sulfide and magnetite dominating. Specifically Fe is dominantly present as Fe(II) prior to reaction with the fracture fluid, and "hot spots" are dominated by pyrite or pyrrhotite. The only detectable Fe(III)-bearing phase in hot spots was magnetite (**Figure 3**). Notably, the only unreacted sample with detectable Fe(III)-(oxy)hydroxides (from bulk EXAFS data) is the unreacted Barnett shale core collected from a depth of 2613 m (**Table 4**). Based on direct measurements of Fe mineralogy and oxidation, the absence of oxidized Fe in unreacted outcrop samples demonstrates that the outcrop samples considered here are not more oxidized than core samples of Marcellus and Green River shales.

Impact of Dissolved Oxygen on Iron Reactivity - The presence of dissolved O_2 is necessary for the oxidation of dissolved Fe in these shale systems. In reactors where O_2 was removed from both the solution and headspace by sparging with Ar gas, none of the released Fe oxidized. The use of oxygenated fluid for these reactors mirrors industrial hydraulic fracturing, where the removal of dissolved O_2 from the injection fluids, either chemically or by sparging, is either ineffective and/or not regularly performed. As a consequence, dissolved O_2 in fluids injected into the subsurface is initially in equilibrium with atmospheric pO_2. Although there is a slight chance that sample contamination occurred, Zolfaghari *et al.* (2016) showed that produced waters from hydraulic fracturing of shales in Canada still contain dissolved O_2 at concentrations near 9 mg/L[29]. Even with significant quantities of dissolved O_2 in the shale reactors, the Fe that is released from the shale, primarily from pyrite, is slow to oxidize due to the low pH of the solution[38].

Impact of pH on Fe Release and Oxidation Rates - In the shale-hydraulic fracture fluid system, HCl has the greatest influence on Fe release from shale. At the lower pH values of the Barnett and Marcellus reactors (pH < 4.0), the rate of oxidation of released Fe(II) is expected to be ~3.2 orders of magnitude slower than at pH 7.0[38] (**Figure 11**). As a consequence of this slow oxidation, Fe is present in solution for weeks to months (**Figure 2**). Under these conditions, Fe can be transported away from point sources (pyrite, siderite, Fe-bearing clays, and Fe-bearing phyllosilicates) prior to oxidizing and precipitating at other locations (**Figure 5**).

Fitting the bulk Fe K-edge EXAFS spectra of the Barnett and Marcellus shales resulted in an unexpected conclusion. Because the fraction of the Fe-organic component based on the fits of these spectra either does not change or increases with time, we conclude that Fe(II) associated with the organic component (Fe-Kerogen) is the most stable form of Fe native to the shale and that pyrite is the major source of Fe released during reaction of the shales with fracture fluid (**Table 4**).

Impact of Shale Mineralogy on Rates and Extent of Iron Oxidation- Although O_2 controls the oxidation and precipitation of Fe, it is reactive carbonate abundance that controls the speciation and distribution of the Fe(III)-bearing precipitates. In oil/gas shales that have low carbonate and thus low pH buffering capacities, such as the Marcellus and Barnett shale, the pH values of the systems (at the solid:liquid ratios used in this study) remained low and did not rise to circum-neutral levels (**Table 2 and Figure 1**). In these shales the slow oxidation of aqueous Fe(II) produced highly dispersed Fe(III)-(oxy)hydroxide precipitates occurring at distances greater than 50 μm from Fe(II)-bearing hot spots (**Figures 5A and 5B**).

We found large differences in the μ-XANES spectra at different locations within the reacted Marcellus shale sample (**Figures 5A and 5B**) indicating significant variations in Fe speciation (**Figure 5C**). The linear combination fits of the μ-XANES spectra show that the Fe(II) hot spots (**Figure 5A**) are predominantly pyrite and magnetite, indicating partial oxidation of the pyrite and resulting in a mixed Fe(II/III)-bearing particle being formed in place (**Figure 5D**). In regions at a significant distance from the Fe(II) hot spots (> 20 μm), the Fe phases detected are dominated by ferrihydrite and goethite (**Figures 5B and 5D**).

Eh/pH diagrams were constructed for the Marcellus reactors using Geochemist's Workbench[39] to understand the identity of the dominant Fe phases in the shale reactors at equilibrium. In a situation where the Fe-controlling agents are working effectively, aqueous Fe(II) (either as a hydrated ion or Fe-organic complex) should be the dominant form of Fe in solution over most Eh and pH conditions in the subsurface (**Figure 12A**). However, when Fe-bearing minerals are not suppressed in the thermodynamic modeling, hematite is the most stable Fe(III)-bearing phase in these systems at equilibrium (**Figure 12B**). The relative scarceness of hematite in reacted shales indicates that although hematite is thermodynamically favored, it is kinetically limited in some of these systems. As seen in **Figure 12B,** as dissolved O_2 is consumed and Eh decreases, Fe(II) becomes the predominant Fe species at equilibrium and further precipitation of hematite should cease as long as new oxidants are not introduced to the system. Although the emphasis for the low pH shale systems has been on the Marcellus shale, experimental analyses of the Barnett shale produced similar results, with the exception that goethite, not ferrihydrite, is the dominant Fe(III)-(oxy)hydroxide present (**Table 4**). When Fe(II) oxidizes and precipitates in these systems with low pH buffering capacity, the Fe forms as diffuse Fe(III)-

(oxy)hydroxides that could coat not only fracture surfaces but also pore throats and piping used in hydraulic fracturing operations.

It is surprising that at pH 3 to 4, Fe(II) oxidized and Fe(III)-bearing solids precipitated in the Barnett and Marcellus reactors. The low pH of the system should retard oxidation of iron compared to the circum-neutral conditions of the Eagle Ford and Green River reactors. One possible reason for appreciable oxidation of Fe(II) under these conditions is the presence of dissolved bitumen in solution.

Iron release and precipitate morphology, identity, and distribution differed significantly among different shales at circum-neutral pH. For the carbonate-rich Eagle Ford and Green River shales, little to no Fe was detectable in solution throughout the course of the 3-week, 3-month, and 6-month incubation times, indicating that either no Fe was released from the shale or that the Fe was released, oxidized, and precipitated as a solid too quickly to be detectable in solution (**Figure 2**). The only experiments in which any Fe was detectable was in the Green River reactor at 6 hours of incubation (**Figure 2**). Although the solution data do not indicate that Fe(II) was released and oxidized to Fe(III), XRF mapping shows significantly more Fe(III) in the reacted samples, indicating that Fe(II) was oxidized and precipitated in these carbonate-rich shales. The close proximity of the Fe(III)-bearing phases (predominately hematite) near Fe point sources, primarily pyrite framboids, indicates that released Fe does not travel far once released, resulting in large mineral grains that could easily occlude nano- and micro-pores (**Figure 6**). As seen in the Eagle Ford μ-XRF data (**Figure 6**), the Fe(III)-bearing particles, in this case hematite, can be tens of microns in diameter. These results differ from poorly buffered, low pH systems where Fe(III)-bearing precipitates were dispersed and of lower crystallinity than those of the Eagle Ford and Green River shale systems. These large particles have the potential to impact the porosity, permeability, and fluid movement near the Fe(II) sources, primarily pyrite.

Although there are substantial differences between the low-carbonate and high-carbonate shale-fracture fluid systems examined, there are some similarities. The first similarity is that O_2 is necessary for Fe(II) oxidation in the reactors for both types of system. The second is that in all shales, inorganic Fe species (Fe-sulfides) were more reactive in the presence of fracture fluids, compared to solutions lacking the fracture-fluid additives.

Impact of Bitumen on Fe Oxidation Rates - As **Figure 10** shows, the presence of bitumen can override the retarding effect of low pH on the rates of Fe(II) oxidation. Jones *et al*.[40] showed that in the presence of organics, molecular oxygen can oxidize Fe(II) at lower pH values and that more complex organics, in particular EDTA and fulvic acid, further accelerated oxidation compared to simpler organics, such as citric acid[40]. Bitumen is classified based on three types of organics: asphaltines + saturates, resins, and aromatics[26, 27, 30, 31]. Although many chemicals are

used in dissolving bitumen, 2-ethyl hexanol, which is common to the fracture fluid formulations used in this work, can readily extract bitumen from oil/gas shale[27]. Thus, the release of bitumen in hydraulically fractured subsurface systems can potentially play a significant role in pore fouling and production loss, particularly in systems with low pH buffering capacity.

Conceptual Model of Fe Behavior in Oil/Gas Shale- A conceptual model that integrates these results is presented in **Figure 13**. Iron precipitates, including both distribution and type of phase, are highly dependent on the pH of the solution. Shales with high pH buffering capacity (abundant carbonates) exhibit lower overall release of Fe(II). Because pH is maintained in the near-neutral range, oxidation of released Fe(II) is relatively rapid, with the production of large Fe(III)-(oxyhydr-)oxide grains or grain clusters (tens of microns in diameter) in proximity to the original Fe(II) source, generally pyrite. These large particles will block porosity and inhibit gas flow from the source rock to fracture space. Conversely, in shales where the pH stays low (shale with low pH buffering capacity, or very close to the well bore), released Fe(II) is thermodynamically more stable and is also slower to oxidize. Consequently, it can be transported farther from the Fe source prior to oxidizing and/or precipitating (**Figure 13**). The presence of abundant organics within the shale matrix that can be released by the organics in fracture fluid is likely a key factor contributing to Fe(II) oxidation and subsequent Fe(III)-(oxyhydr-)oxide precipitation at low pH. Although the sizes of these precipitates at lower pH are smaller, they can precipitate farther from the source with the potential of occluding pores, fractures, or wellbore piping far away from the source of Fe in the shale matrix. Our experiments were designed to probe chemical reactions occurring within the first few hours or days of fracture fluid-shale reaction, *i.e.*, during the time period when most of shale alteration occurs and prior to unplugging of the well to allow escape of flowback. However, it is useful to consider how high TDS, present in flowback, might affect our results. For example, recycled flowback or produced water used for new hydraulic fractures is expected to have elevated TDS. Because the reactors in our study used a higher fluid:solid mass ratio than occurs in the field, the total dissolved solids (TDS) concentrations in these reactors are low relative to typical values measured in flowback and produced waters (100's of g/L)[41]. As TDS increases to very high concentrations ~200,000 ppm), the activity of Fe(II) and Fe(III) will decrease significantly due to the formation of ion pairs (including iron-chloride pairs). However, given the high degree of oversaturation in the reactors (calculated saturation indices >5), Fe(III)-(oxyhydr)oxide precipitation is still likely to occur in the subsurface, though at potentially lower quantities and slower rates. With regards to bitumen chemistry, based on the literature, high salinity should have little to no impact on bitumen solubility[27]. The type of organic solvent used in these systems is the most important factor for bitumen extraction from the rock and is relatively independent of salinity. Thus, although our studies provide fundamental insight into the behavior of Fe(II) in shales exposed to hydraulic fracturing fluid, future studies examining the

role of high-TDS fluids would improve our ability to design procedures to improve production in shale reservoirs.

Implications:

Oil/gas shales contain reduced Fe-bearing phases that release Fe(II) in the presence of acid and O_2, which can subsequently be oxidized and result in the formation of Fe(III)-bearing precipitates during hydraulic fracturing. In the four shale samples examined, Fe is associated with a variety of phases: sulfides, clays, oxides, carbonates, and organics. Although there are several potential sources that could release Fe into solution, EXAFS spectroscopy shows that pyrite is more reactive with hydraulic fracture fluid than Fe(II) bound to organics. Reaction of the shale samples with hydrochloric acid is necessary for the release of Fe into solution. However, dissolved O_2 is critical for the oxidation of Fe(II) to Fe(III). At low pH, oxidation of Fe(II) to Fe(III) is generally slow; however, we found that bitumen released from the shale by the organics in fracture fluid reduces the inhibiting effect of hydrochloric acid on Fe(II) oxidation and enhances oxidation at pH = 2.0. Thus bitumen in shale systems with low buffering capacity (*i.e.* low concentrations of carbonate minerals) can play a major role in the formation of Fe(III)-bearing precipitates that would otherwise not be expected to form. One aspect that was not studied here is the potential impact of microorganisms in the subsurface on the cycling of Fe. The dominant microbial groups present in the subsurface, in descending order of abundance, are H_2S producers, anaerobic fermenters, and methanogens[42, 43]. Because of the high abundance of H_2S producers, there is the potential that a portion of the released Fe(II) reacts with H_2S to precipitate Fe-sulfides (mackinawite) prior to oxidation. Although this is a possibility, the impact is probably quite minor due to the presence of dissolved O_2 and biocides injected into the subsurface that inhibit or kill H_2S-producing bacteria and the high reactivity of mackinawite in the presence of O_2.

The importance of the pH buffering capacity of shales on the oxidation and precipitation of Fe-bearing solids can not be overstated in the context of this study and is consistent with results of a companion paper by Harrison *et al.* (*accepted*) as well as work by Wilke *et al.*[44]. In systems with low pH buffering capacity (*e.g.*, Marcellus and Barnet shales), released Fe(II) can stay in solution for a significant amount of time, allowing diffusion and transport of Fe(II) to occur prior to oxidation and precipitation of Fe(III)-bearing solids. When Fe(II) oxidation does occur in carbonate-poor systems, the resultant Fe(III)-bearing precipitates are distributed in a diffuse fashion and occur at significant distances from the Fe(II) point sources. These precipitates tend to be comprised of ferrihydrite and goethite. The potential for transport of Fe released from oil/gas shales can result in occlusion of pores, pore necks, and piping used in the hydraulic

fracturing process, which could (and most likely does) reduce production with time. In contrast, in shales with high buffering capacity (Green River and Eagle Ford), released Fe(II) is quickly oxidized and remains in close proximity to the point source.

Conclusions:

Our study of both well pH-buffered and poorly pH-buffered shale systems provides persuasive evidence that oxidation and redistribution of Fe may play important roles in the rapid decrease of hydrocarbon production with time that is observed in active wells following hydraulic fracturing. Our study also shows that even though ethylene glycol (Fe-controlling agent) injected into the subsurface can have an impact on Fe precipitation, this chemical appears to be only partially effective in controlling Fe in solution. These findings indicate that additional research on the types of chemicals injected, injection sequences, and the control of both acid and dissolved O_2 is needed to control the behavior of Fe during hydraulic fracturing of oil/gas shales. Such control could have the potential to increase both hydrocarbon production and the efficiency of re-fracturing oil/gas shales, which could increase the utility of an already vital portion of the energy portfolio of the United States.

Acknowledgments:

We would like to thank Dr. Arjun Kholi of Stanford University for providing the Eagle Ford and Barnett shale samples used in this work. We would also like to thank Drs. Sam Webb and Courtney Roach (SSRL) for helping with XRF and μ-XANES data collection on beamline 2-3 and Ryan Davis (SSRL) for assistance in collecting the Fe bulk EXAFS data on beamline 4-1. Additional thanks go to Drs. Vincent Noel and Naresh Kumar of Stanford University plus Dr. Jason Stuckey of University of Delaware for providing Fe EXAFS reference spectra used in fitting of the x-ray absorption spectra in this study. We would also like to thank the staff of the Stanford Nano Shared Facility for help with SEM imaging. We gratefully acknowledge the funding for this project provided via a grant by the National Energy Technology Laboratory to SLAC under Contract #DE-AC02-765F00515.

Literature Cited:

1. Wang, Z.; Krupnick, A. *A Retrospective Review of Shale Gas Development in the United States*; Resources for the Future: Washington D.C., 2013; p 42.
2. Zhang, P.; Hu, L.; Meegoda, J. N.; Gao, S., Micro/Nano-pore Network Analysis of Gas flow in Shale Matrix. *Nature Scientific Reports* **2015,** 5, 1-11.
3. Bustin, A. M. M.; Bustin, R. M., Importance of rock properties on the producibility of gas shales. *International Journal of Coal Geology* **2012,** 103, 132-147.
4. Patzek, T. W.; Male, F.; Marder, M., Gas production in the Barnett Shale obeys a simple scaling theory. *Proceedings of the National Academy of Science* **2013,** 110, (49), 19731-19736.
5. Monteiro, P. J. M.; Rycroft, C. H.; Barenblatt, G. I., A Mathematical Model of Fluid and Gas Flow in Nanoporous Media. *Proceedings of the National Academy of Science* **2013,** 109, (50), 20309-20313.
6. Liu, J.; Wang, J. G.; Gao, F.; Ju, Y.; Zhang, X.; Zhang, L.-C., Flow Consistency Between Non-Darcy Flow in Fracture Network and Nonlinear Diffusion in Matrix to Gas Production Rate in Fractured Shale Gas Reservoirs. *Transport in Porous Media* **2016,** 111, 97-121.
7. Falk, K.; Coasne, B.; Pellenq, R.; Ulm, F.-J.; Bocquet, L., Subcontinuum Mass Transport of Condensed Hydrocarbons in Nanoporous Media. *Nature Communications* **2015,** 6, 1-7.
8. Karra, S.; Makedonska, N.; Viswanathan, H. S.; Painter, S. L.; Hyman, J. D., Effect of Advective Flow in Fractures and Matrix Diffusion on Natural Gas Production. *Water Resources Research* **2015,** 51, 8646-8657.
9. Chermak, J. A.; Schreiber, M. E., Mineralogy and Trace Element Geochemistry of Gas Shales in the United States: Environmental Implications. *International Journal of Coal Geology* **2014,** 126, 32-44.
10. Ground Water Protection Council; Interstate Oil & Gas Compact Commission. FracFocus Chemical Disclosure Registry. **2016**.
11. Abualfaraj, N.; Gurian, P. L.; Olson, M. S., Characterization of Marcellus Shale Flowback Water. *Environmental Engineering Science* **2014,** 31, (9), 514-524.
12. Balashov, V. N.; Engelder, T.; Gu, X.; Fantle, M. S.; Brantley, S. L., A Model Describing Flowback Chemistry Changes with Time After Marcellus Shale Hydraulic Fracturing. *AAPG Bulletin* **2015,** 99, (1), 143-154.
13. Ghanbari, E.; Dehghanpour, H., The Fate of Fracturing Water: A Field and Simulation Study. *Fuel* **2016,** 163, 282-294.
14. Lester, Y.; Ferrer, I.; Thurman, E. M.; Sitterley, K.; Korak, J. A.; Aiken, G.; Linden, K. G., Characterization of Hydraulic Fracturing flowback Water in Colorado: Implications for Water Treatment. *Science of the Total Environment* **2015,** 512-513, 637-644.
15. Munirasu, S.; Haija, M. A.; Banat, F., Use of Membrane Technology for Oil Field and Refinery Produced Water Treatment-A Review. *Process Safety and Environmental Protection* **2016,** 100, 183-202.
16. Vikram, A.; Lipus, D.; Bibby, K., Produced Water Exposure Alters Bacterial Response to Biocides. *Environmental Science & Technology* **2014,** 48, 13001-13009.
17. Wang, L.; Fortner, J. D.; Giammar, D. E., Impact of Water Chemistry on Element Mobilization from Eagle Ford Shale. *Environmental Engineering Science* **2015,** 32, (4), 310-320.
18. Chalmers, G. R.; Bustin, R. M.; Power, I. M., Characterization of Gas Shale Pore Systems by Porosimetry, Pycnometry, Surface Area, and Field Emission Scanning Electron Microscopy/Transmission Electron Microscopy Image Analyses: Examples from the Barnett, Woodford, Haynesville, Marcellus, and Doig Units. *AAPG Bulletin* **2012,** 96, (6), 1099-1119.

19. Curtis, M. E.; Sondergeld, C. H.; Ambrose, R. J.; Rai, C. S., Microstructural Investigation of Gas Shales in Two and Three Dimensions Using Nanometer-scale Resolution Imaging. *AAPG Bulletin* **2012,** 96, (4), 665-677.
20. Davies, R. J.; Mathias, S. A.; Moss, J.; Hustoft, S.; Newport, L., Hydraulic Fractures: How Far Can They Go? *Marine and Petroleum Geology* **2012,** 37, 1-6.
21. Gale, J. F. W.; Laubach, S. E.; Olson, J. E.; Eichhubl, P.; Fall, A., Natural Fractures in Shale: A Review and New Observations. *AAPG Bulletin* **2014,** 98, (11), 2165-2216.
22. Gale, J. F. W.; Reed, R. M.; Holder, J., Natural Fractures in the Barnett Shale and Their Importance for Hydraulic Fracture Treatments. *AAPG Bulletin* **2007,** 91, (4), 603-622.
23. Hammack, R. W.; Harbert, W.; Sharma, S.; Stewart, B. W.; Capo, R. C.; Wall, A. J.; Wells, A.; Diehl, R.; Blaushild, D.; Sams, J.; Veloski, G. *An Evaluation of Fracture Growth and Gas/Fluid Migration as Horizontal Marcellus Shale Gas Wells are Hydraulically Fractured in Greene County, Pennsylvania*; National Energy Technology Laboratory: Pittsburgh, 2014; p 76.
24. Harris, W. M.; Chiu, W. K. S., Determining the Representative Volume Element Size for Three-dimensional Microstructural Material Characterization. Part 1: Predictive Models. *Journal of Power Sources* **2015,** 282, 552-561.
25. Milliken, K. L.; Rudnicki, M.; Awwiller, D. N.; Zhang, T., Organic Matter-hosted Pore System, Marcellus Formation (Devonian), Pennsylvania. *AAPG Bulletin* **2013,** 97, (2), 177-200.
26. Loeber, L.; Muller, G.; Morel, J.; Sutton, O., Bitumen in Colloid Science: A Chemical, Structural and Rheological Approach. *Fuel* **1998,** 77, (13), 1443-1450.
27. Redelius, P. G., Solubility Parameters and Bitumen. *Fuel* **2000,** 79, 27-35.
28. Goklen, K. E.; Stoecker, T. J.; Baddour, R. F., A Method for the Isolation of Kerogen from Green River Oil Shale. *Industrial & Engineering Chemistry Product Research and Development* **1984,** 23, 308-311.
29. Zolfaghari, A.; Dehghanpour, H.; Noel, M.; Bearinger, D., Laboratory and Field Analysis of Flowback Water from Gas Shales. *Journal of Unconventional Oil and Gas Resources* **2016,** 14, 113-127.
30. Redelius, P.; Soenen, H., Relation Between Bitumen Chemistry and Performance. *Fuel* **2015,** 140, 34-43.
31. Traxler, R. N., The Physical Chemistry of Asphaltic Bitumen. *Chemical Reviews* **1936,** 19, (2), 119-143.
32. Materials Data, Inc. *Jade XRD Pattern Processing Ver. 6.5*, **2002**.
33. Webb, S. *SMAK: Sam's Microprobe Analysis Kit Ver. 0.50*, **2006**.
34. Webb, S. *SixPACK*, 0.63; Stanford Synchrotron Radiation Laboratory: Menlo Park, **2006**.
35. Webb, S. M., SIXPack: a graphical user interface for XAS analysis using IFEFFIT. *Physica Scripta* **2005,** T115, 1011-1014.
36. Kruger, C.; Barnett, B. L.; Brauer, D., *The Organic Chemistry of Iron: Volume I*. Academic Press: New York, **1978**; p 672.
37. Ankudinov, A. L.; Ravel, B.; Rehr, J. J.; Conradson, S. D., Real-space Multiple-scattering Calculation and Interpretation of X-ray Absorption Near-edge Structure. *Physica Review B* **1998,** 58, (12), 7565-7576.
38. Morgan, B.; Lahav, O., The effect of pH on the kinetics of spontaneous Fe(II) oxidation by O_2 in aqueous solution - basic principles a simple heuristic description. *Chemosphere* **2007,** 68, (11), 2080-2084.
39. *The Geochemist's Workbench* 8.0; Aqueous Solutions, LLC: **2009**.
40. Jones, A. M.; Griffin, P. J.; Waite, T. D., Ferrous Iron Oxidation by Molecular Oxygen Under Acidic Conditions: The Effect of Citrate, EDTA and Fulvic Acid. *Geochimica et Cosmochimica Acta* **2015,** 160, 117-131.

41. Haluszczak, L. O.; Rose, A. W.; Kump, L. R., Geochemical evaluation of flowback brine from Marcellus gas wells in Pennsylvania, USA. *Applied Geochemistry* **2013,** 28, 55-61.
42. Cluff, M. A.; Hartsock, A.; MacRae, J. D.; Carter, K.; Mouser, P. J., Temporal Changes in Microbial Ecology and Geochemistry in Produced Water from Hydraulically Fractured Marcellus Shale Gas Wells. *Environmental Science & Technology* **2014,** 48, 6508-6517.
43. Akob, D. M.; Cozzarelli, I. M.; Dunlap, D. S.; Rowan, E. L.; Lorah, M. M., Organic and Inorganic Composition and Microbiology of Produced Waters from Pennsylvania Shale Gas Wells. *Applied Geochemistry* **2015,** 60, 116-125.
44. Wilke, F. D. H.; Vieth-Hillebrand, A.; Naumann, R.; Erzinger, J.; Horsfield, B., Induced Mobility of Inorganic and Organic Solutes from Black Shales using Water Extraction: Implications for Shale Gas Exploitation. *Applied Geochemistry* **2015,** 63, 158-168.
45. McKibben, M. A.; Barnes, H. L., Oxidation of pyrite in low temperature acidic solutions: Rate laws and surface textures. *Geochimica et Cosmochimica Acta* **1986,** 50, 1509-1520.

Ingredient	Purpose	By Mass	Percentage of Ingredient (wt.%)
Water	Base Fluid	1995.6674 g	99.783%
Ethylene Glycol	Scale Inhibitor, Iron Control, Breaker	0.4113 g	0.021%
Kerosene	Friction Reducer	0.4815 g	0.024%
Guar Gum	Dry Gellant	0.5807 g	0.029%
2-Ethyl hexanol	Corrosion Inhibitor for Acid	0.0093 g	0.0005%
Glycol ether	Corrosion Inhibitor for Acid	0.0031 g	0.0002%
Polyethylene glycol	Biocide	0.3974 g	0.020%
Hydrochloric acid	Acid	2.4493 g	0.122%

Table 1: Fracture-fluid composition used in experiments based on reported additives used at Marcellus Shale gas Well E. Silica Proppant and two biocides (2,2-Dibromo-3-nitrilopropionamide and Dibromoacetonitrile) were removed from the formulation. Polyethylene glycol represents more than 60% of the total biocide introduced into Well E. Solution pH = 2.00

Sample	Quartz	Calcite	Dolomite	Illite	Kaolinite	Pyrite	Feldspar	Analcime
Barnett Initial	44.2	8.2	X	40.6	X	2.1	4.9	X
Barnett 3 Week	68.4	X	X	29.1	X	2.5	X	X
Barnett 3 Week Dup	65.9	X	X	31.9	X	2.2	X	X
Barnett 3 Month	68.2	X	X	29.0	X	2.8	X	X
Barnett 6 Month	64.1	X	X	33.8	X	2.1	X	X
Marcellus Initial	42.2	11.6	1.1	35.0	X	6.4	3.7	X
Marcellus 3 Week	66.0	X	X	28.1	X	5.9	X	X
Marcellus 3 Month	60.6	X	X	34.3	X	5.1	X	X
Marcellus 3 Month Dup	61.3	X	X	33.4	X	5.3	X	X
Marcellus 6 Month	52.0	X	X	43.8	X	4.2	X	X
Marcellus 3 Week No O_2	59.7	X	X	34.9	X	5.4	X	X
Eagle Ford Initial	25.2	64.5	X	X	7.6	2.7	X	X
Eagle Ford 3 Week	34.3	54.0	X	X	7.7	4.0	X	X
Eagle Ford 3 Month	36.4	52.5	X	X	7.3	3.8	X	X
Eagle Ford 6 Month	36.5	52.8	X	X	7.9	2.8	X	X
Green River Initial	31.4	23.2	28.9	X	X	X	8.0	8.5
Green River 3 Week	23.3	17.7	41.9	9.2	X	X	4.3	3.6
Green River 3 Month	23.3	20.2	36.9	11.2	X	X	5.3	3.1
Green River 6 Month	23.4	19.3	40.3	9.5	X	X	4.3	3.2

Table 2: Quantitative XRD results of sand-sized oil/gas shale samples. Quantitative results are derived from least-squares fitting of the data using the JADE diffraction software. All values are in wt.% with "X" denoting a non-detect for the phase. Uncertainty for fits to phases is ≤ 15%, detection limit is 0.1 wt.%.

Sample	Na (wt.%)	K (wt.%)	Ca (wt.%)	Mg (wt.%)	Al (wt.%)	Si (wt.%)	Fe (mg/g)	TC (wt.%)
Barnett Initial	0.103	1.646	2.509	0.631	7.291	25.53	24.83	16.00
Barnett 3 Week	0.115	1.882	0.136	0.348	7.674	28.64	20.79	4.29
Barnett 3 Week Dup	0.089	1.811	0.090	0.486	10.28	34.52	20.51	4.44
Barnett 3 Month	< 0.01	1.763	0.064	0.321	7.081	25.86	18.99	4.56
Barnett 6 Month	< 0.01	1.447	0.054	0.457	10.81	34.91	15.36	4.60
Marcellus Initial	< 0.01	2.069	4.227	0.784	10.5	28.41	45.63	6.04
Marcellus 3 Week	< 0.01	1.872	2.781	0.589	6.535	21.04	36.88	5.86
Marcellus 3 Month	< 0.01	2.098	0.073	0.792	11.02	31.97	30.38	5.77
Marcellus 3 Month Dup	< 0.01	2.105	0.151	0.498	7.17	23.78	32.55	5.76
Marcellus 6 Month	< 0.01	2.328	0.251	0.574	8.003	26.20	37.60	6.05
Marcellus 3 Week No O_2	< 0.01	3.023	0.019	0.719	8.757	25.16	40.96	6.18
Eagle Ford Initial	< 0.01	0.886	16.67	0.371	5.818	15.97	21.17	4.42
Eagle Ford 3 Week	< 0.01	0.979	13.46	0.468	6.376	17.93	23.93	9.90
Eagle Ford 3 Month	< 0.01	1.025	12.87	0.469	6.232	18.14	22.45	8.84
Eagle Ford 6 Month	< 0.01	0.882	10.49	0.412	5.306	15.42	19.26	9.99
Green River Initial	0.943	1.074	13.64	4.414	2.662	12.27	17.83	12.71
Green River 3 Week	1.012	1.399	13.08	4.43	3.632	15.97	22.15	13.44
Green River 3 Month	0.874	1.184	9.108	3.696	2.76	17.93	13.61	12.29
Green River 6 Month	0.856	1.121	10.23	3.50	2.991	12.85	17.50	11.99

Table 3: Bulk XRF measurements of selected elements for sand-sized oil/gas shale samples. Uncertainty for triplicate measurements is ≤ 5%, 1 SD. Total Carbon (TC) was analyzed using Dumas combustion.

Barnett Sample	**Pyrite**	**Goethite**	**Fe-Organics**	**Residual**			
Initial	0.67	0.21	0.12	0.721			
3 Week	0.72	0.12	0.16	0.758			
3 Week Duplicate	0.69	0.15	0.16	0.772			
3 Month	0.75	0.11	0.14	0.938			
6 Month	0.69	0.13	0.18	0.681			
Marcellus Sample	**Pyrite**	**Ferrihydrite**	**Hornblende**	**Biotite**	**Fe-Organics**	**Residual**	
Initial	0.53	X	0.08	0.26	0.13	0.840	
3 Week	0.64	0.16	X	X	0.20	0.915	
3 Month	0.65	0.20	X	X	0.15	0.874	
3 Month Duplicate	0.64	0.18	X	X	0.18	0.965	
6 Month	0.62	0.11	X	X	0.27	0.529	
Eagle Ford Sample	**Pyrite**	**Ferrihydrite**	**Goethite**	**Hematite**	**Siderite**	**Fe-Organics**	**Residual**
Initial	0.92	X	X	X	0.08	X	0.987
3 Week	0.61	X	0.20	X	X	0.19	0.752
3 Month	0.65	X	0.18	X	X	0.17	0.862
6 Month	0.47	X	X	0.20	X	0.33	0.793
Green River Sample	**GR Initial Shale**	**GR 3 Week Reacted Shale**	**GR 3 Week Reacted Kerogen**	**Residual**			
3 Week	0.55		0.45	0.706			
3 Month		0.40	0.60	0.320			
6 Month		0.40	0.60	0.264			

Table 4: Results of linear combination fitting of the bulk Fe K-edge EXAFS for sand-sized oil/gas shale samples. The Fe-C component was fit using an Fe-humate reference spectrum. Uncertainty for all fitting components is ≤ 10%, 1 SD. Non-detects are denoted as X.

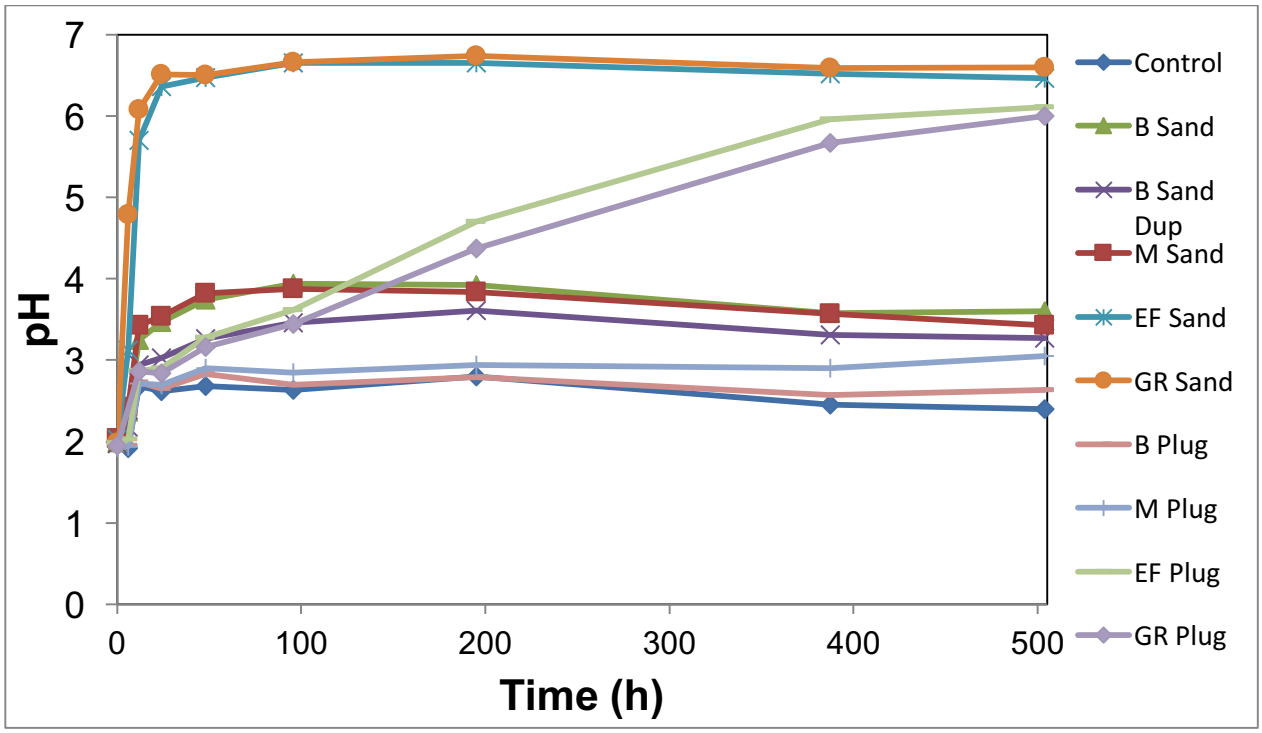

Figure 1: pH measurements of 3 week reactors for all four shale samples. M = Marcellus, B = Barnett, EF = Eagle Ford, and GR = Green River. Control contains all fracture fluid components but no shale material. Plug, refers to whole shale pieces that are not ground. Uncertainty in triplicate measurements is less than 0.05 pH units.

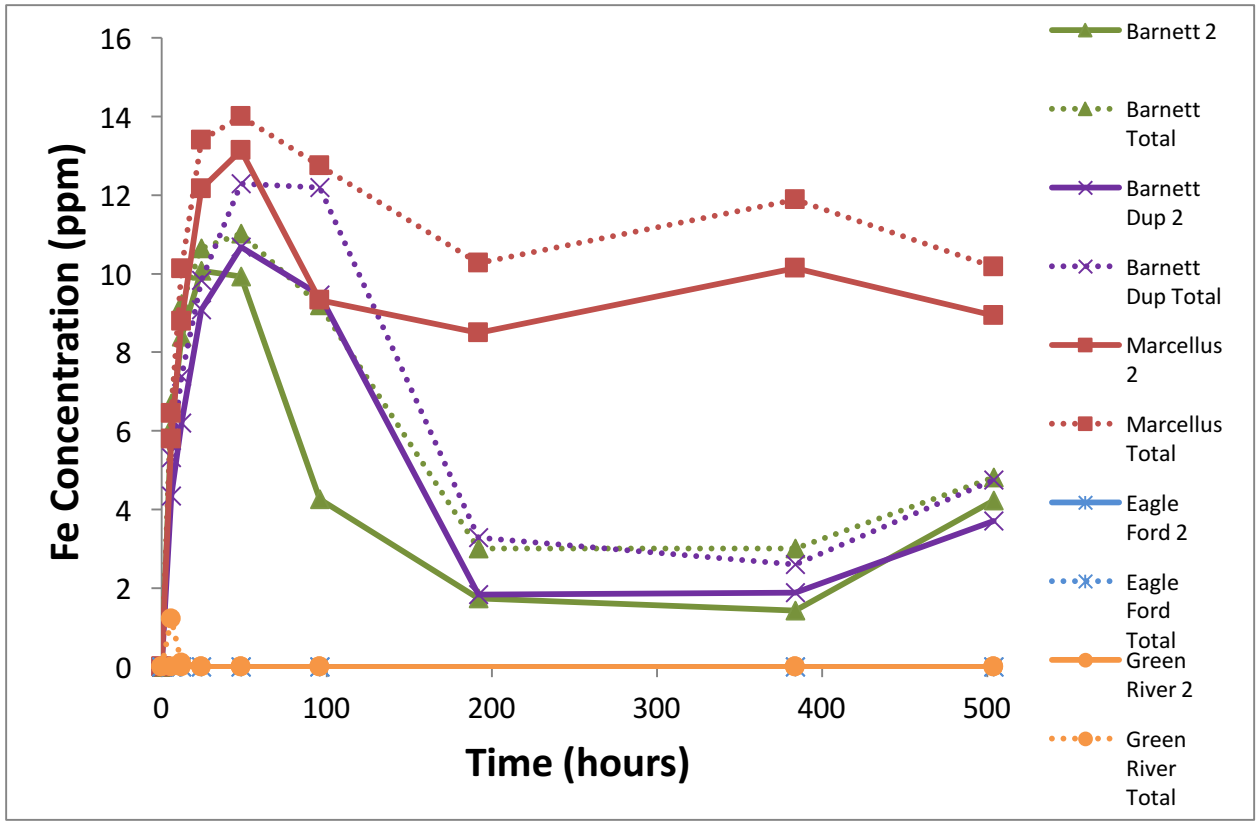

Figure 2: Iron release curve from sand-sized shale samples. The number "2" denotes Fe(II) concentrations while "Total" denotes total Fe concentrations in solution. Uncertainty in triplicate samples is < 8%.

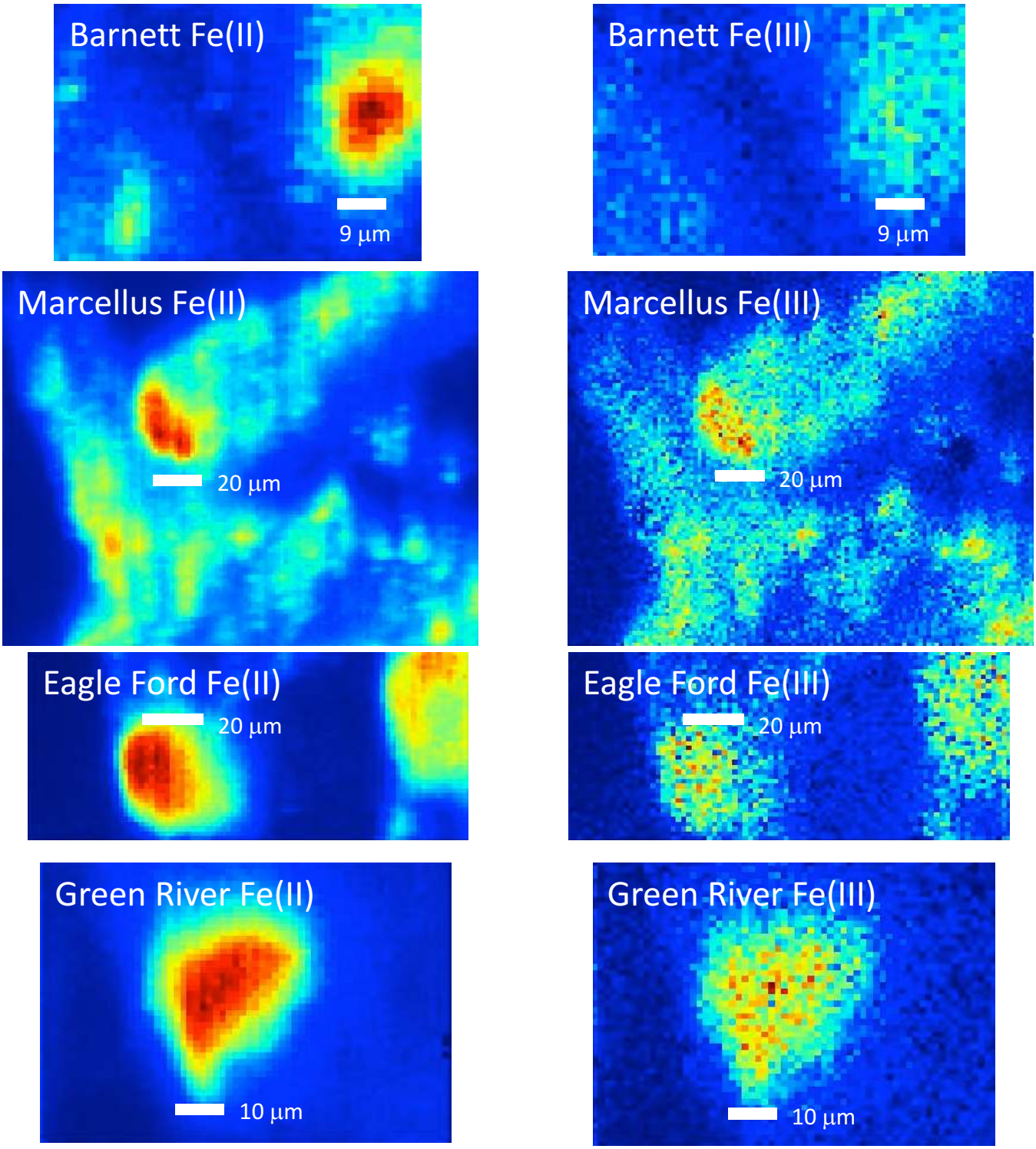

Figure 3: Iron K-edge synchrotron μ-XRF imaging of the initial oil/gas shale sand-sized samples. Pyrite is the dominant Fe(II)-bearing phase for Barnett, Eagle Ford, and Marcellus with Fe(III) rich regions being almost exclusively magnetite. Pyrrhotite is the primary Fe(II)-bearing phase for Green River with magnetite being the primary Fe(III)-bearing phase.

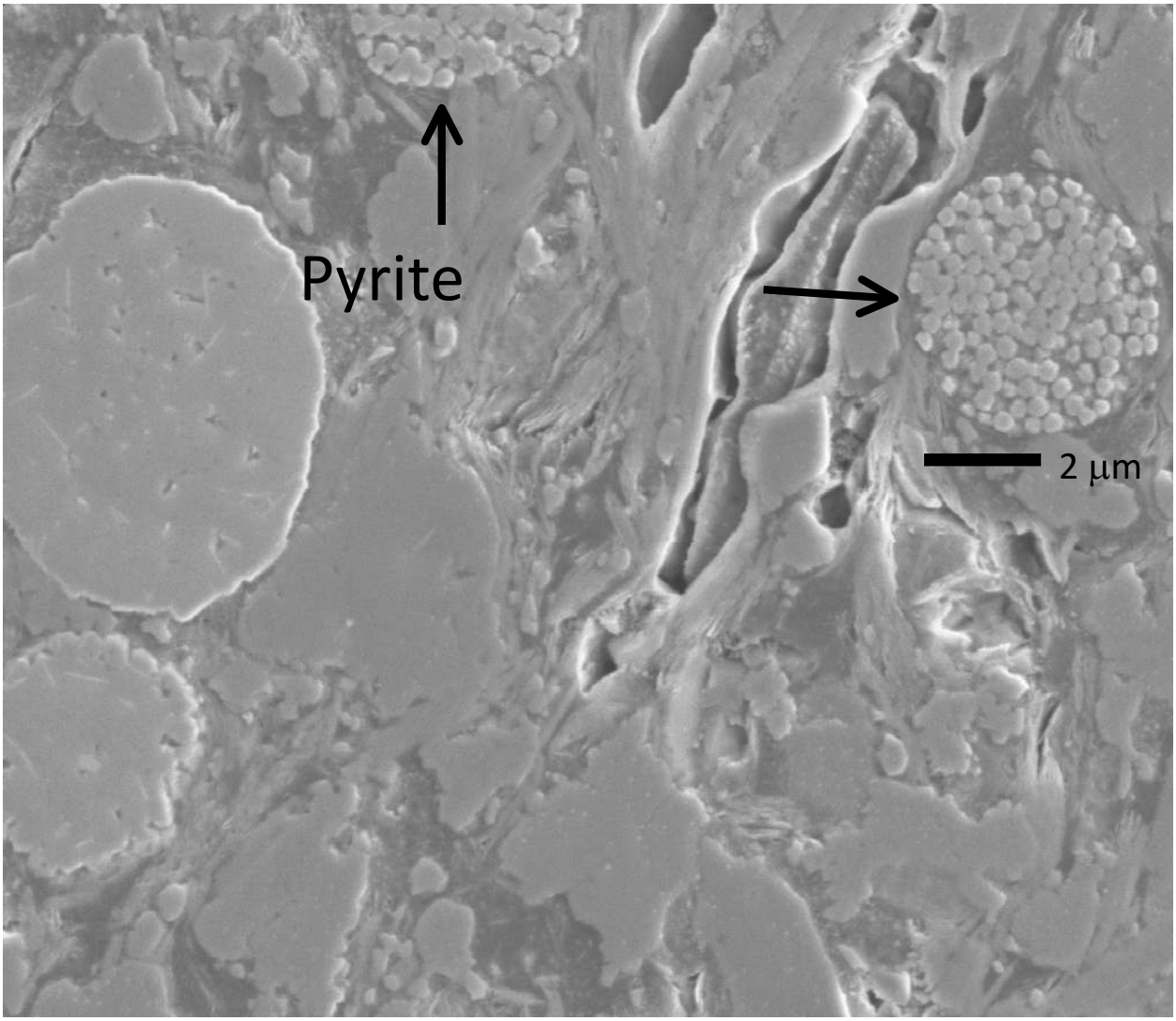

Figure 4: Scanning electron microscope image of unreacted Marcellus shale showing framboidal pyrites; image collected from sand-sized shale sample.

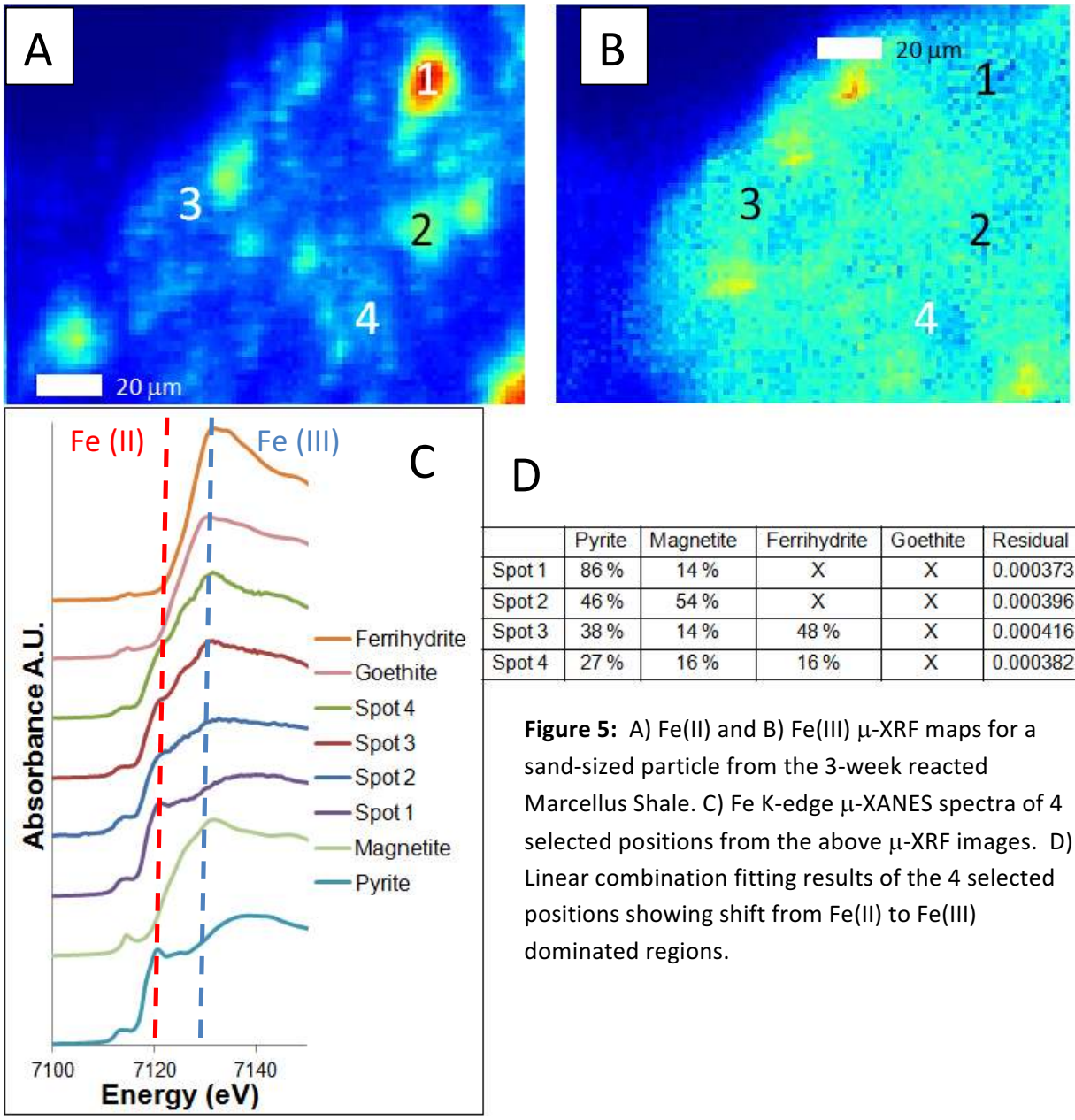

D

	Pyrite	Magnetite	Ferrihydrite	Goethite	Residual
Spot 1	86 %	14 %	X	X	0.000373
Spot 2	46 %	54 %	X	X	0.000396
Spot 3	38 %	14 %	48 %	X	0.000416
Spot 4	27 %	16 %	16 %	X	0.000382

Figure 5: A) Fe(II) and B) Fe(III) µ-XRF maps for a sand-sized particle from the 3-week reacted Marcellus Shale. C) Fe K-edge µ-XANES spectra of 4 selected positions from the above µ-XRF images. D) Linear combination fitting results of the 4 selected positions showing shift from Fe(II) to Fe(III) dominated regions.

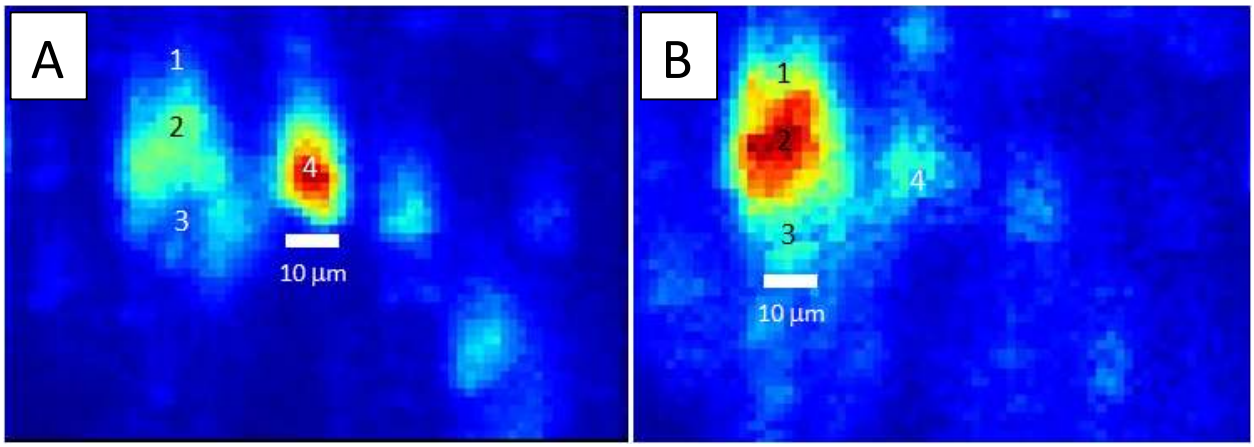

	Pyrite	Pyrrhotite	Magnetite	Hematite	Residual
Spot 1	19 %	X	37 %	45 %	0.002858
Spot 2	12 %	X	37 %	51 %	0.003642
Spot 3	41 %	X	36 %	23 %	0.000165
Spot 4	54 %	34 %	12 %	X	0.000677

Figure 6: A) Fe(II) and B) Fe(III) µ-XRF maps for a sand-sized particle from the 3-week reacted Eagle Ford Shale. C) Linear combination fitting results of the 4 selected positions showing shift from Fe(II) to Fe(III) dominated regions with the presence of significant quantities of hematite. Non-detects are denoted as "X".

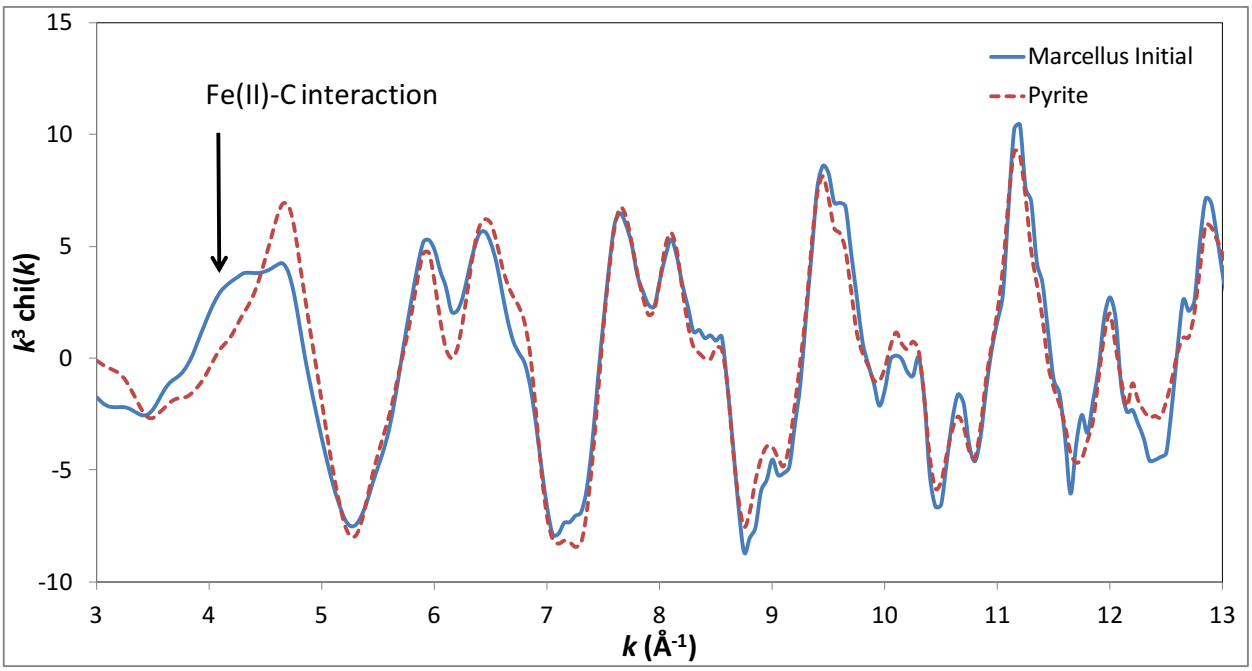

Figure 7: Bulk Fe K-edge EXAFS of the Marcellus shale prior to reaction with hydraulic fracturing fluid. The dashed line is a pyrite reference compound illustrating that the majority of the features are due to pyrite. The feature at k = 4 is not consistent with any inorganic Fe compound in the reference library. Shell-by-shell fitting of the data indicates that the feature at k = 4 is consistent with an Fe(II)/C interaction at 2.11 Å.

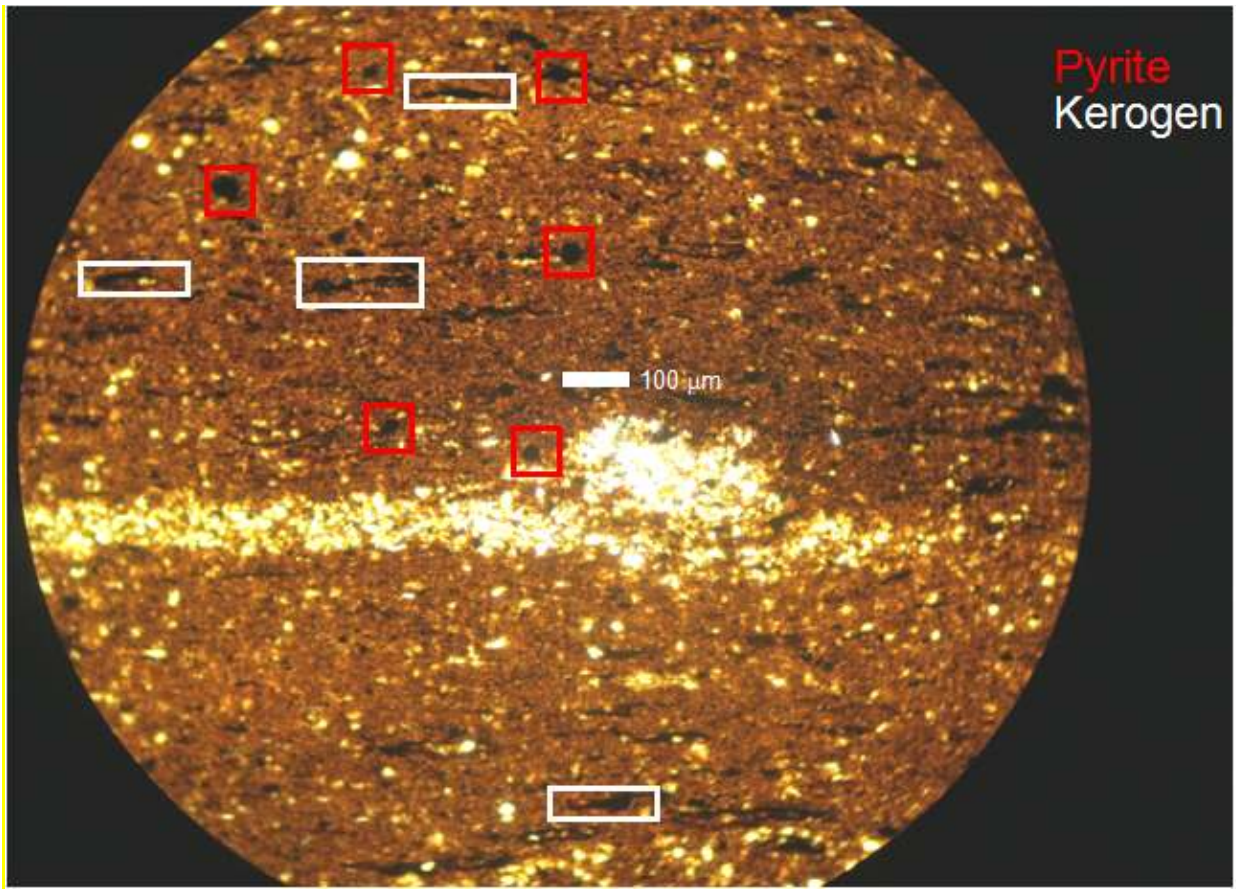

Figure 8: Petrographic thin section cut from a large piece of Marcellus shale (original block was 20 cm x 20 cm x 10 cm) under plain polarized light, thin section was cut perpendicular to bedding. The white boxes illustrates the typical morphology and high abundance of kerogen in the shale while the red boxes indicates typical morphology of pyrite. White minerals in the thin section are quartz crystals while the brown colored matrix material is mostly clay minerals.

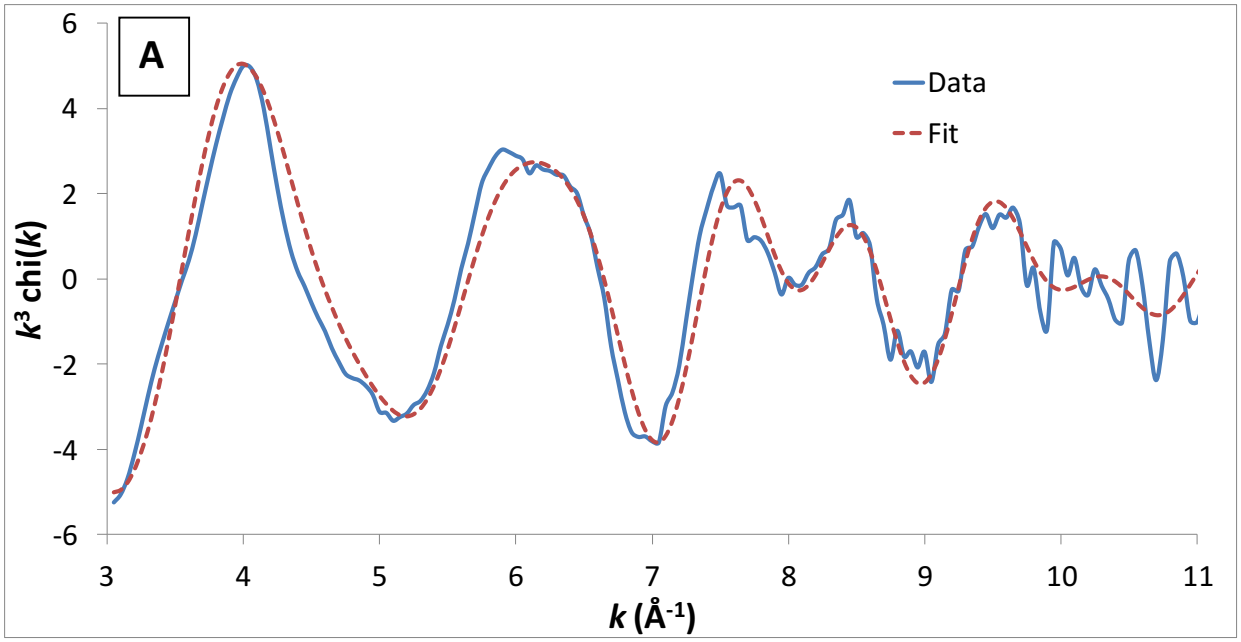

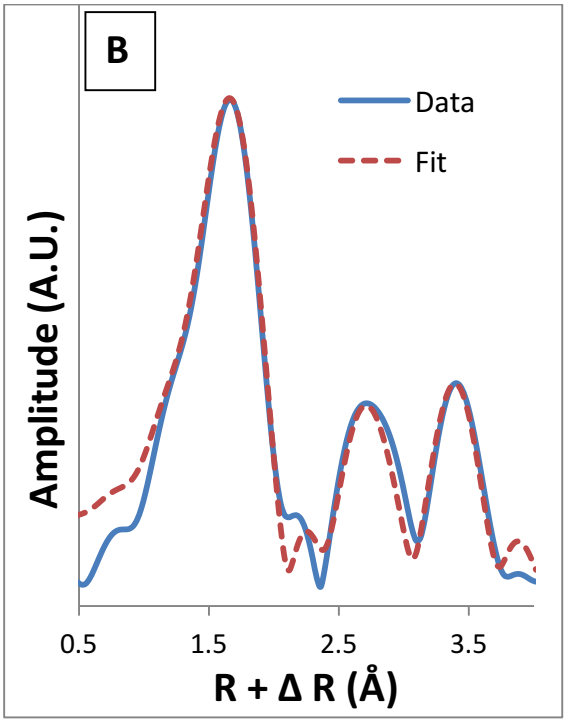

Pathway	CN	R	σ^2
Fe-C	7.45 ± 0.36	2.11 ± 0.02	0.010 ± 0.001
Fe-S	1.93 ± 0.30	3.22 ± 0.01	0.008 ± 0.001
Fe-Fe	1.31 ± 0.21	3.82 ± 0.01	0.005 ± 0.001
E_0	-0.118 ± 0.425	Red Chi sq	7.81
$S0^2$	0.896 ± 0.040	R Factor	0.0294

Figure 9: Shell-by-shell fitting of Fe K-edge EXAFS data for Green River Shale, unreacted. A) Fit of EXAFS data using Fe(II)-C pathway along with the Fe-S and Fe-Fe pathways of pyrite/pyrrhotite. B) Fit of the Fourier Transform.

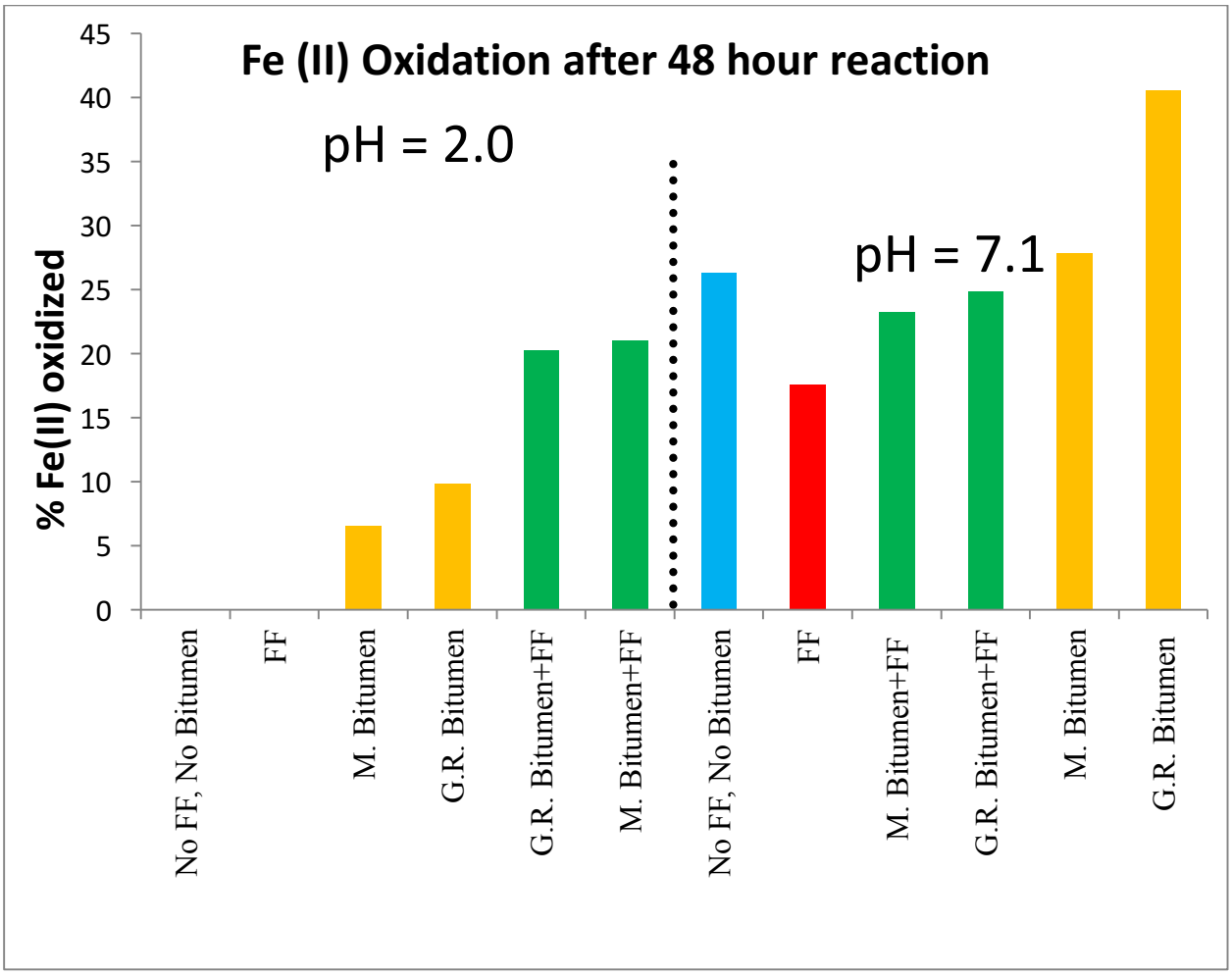

Figure 10: Percentage of Fe(II) oxidized in idealized Fe reactors over a 48 hour period at two different solution pHs with and without the presence of bitumen. FF stands for Fracture Fluid, while M. stands for Marcellus and G.R. stands for Green River.

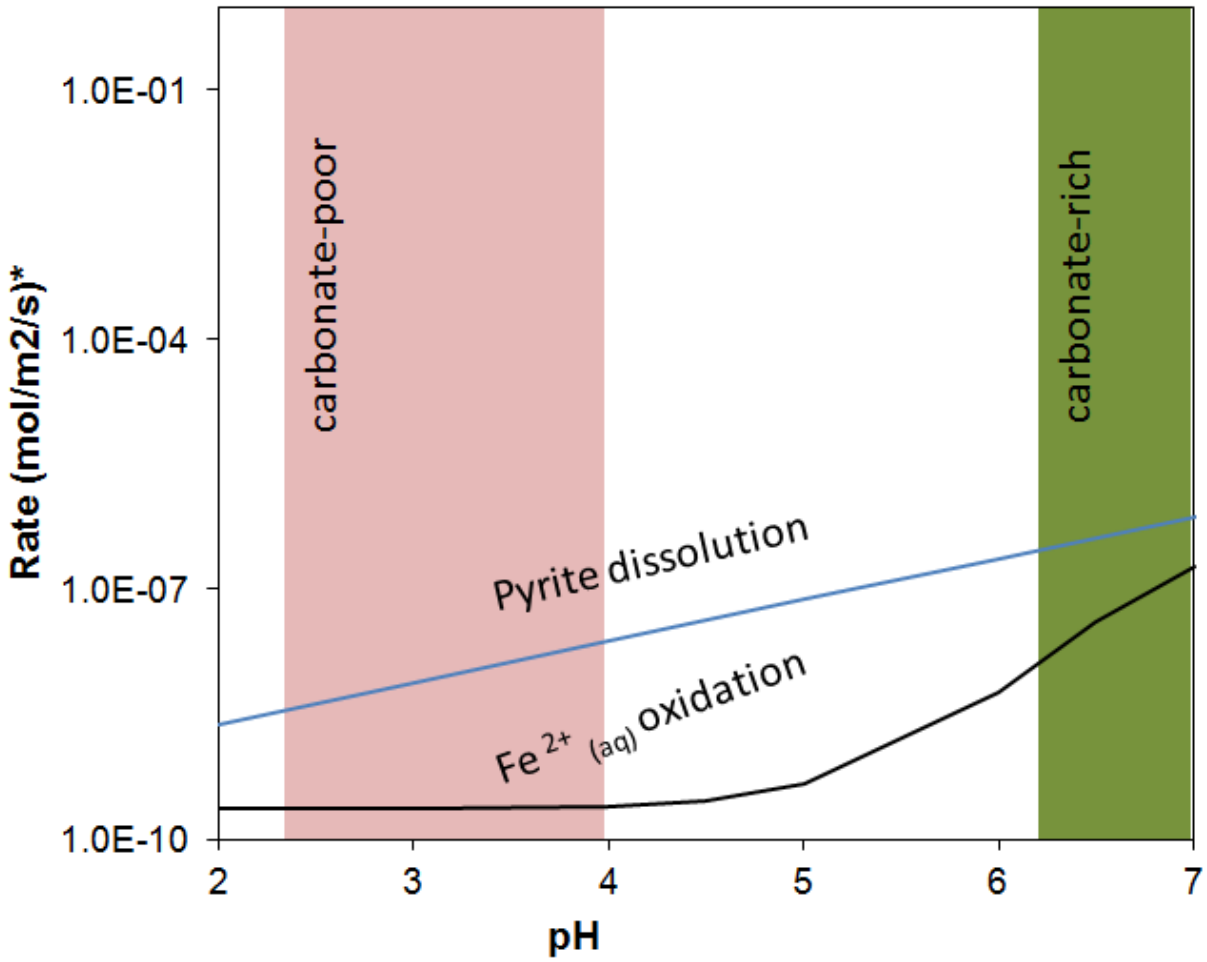

Figure 11: Conceptual diagram of relative rates of pyrite dissolution and Fe(II) oxidation as a function of pH. Pyrite dissolution rates were calculated using a rate law from McKibben and Barnes[45] at 30°C with a fixed Fe(III) concentration of 6.12 x 10^{-5} mol/L and a rate constant of 3.0 mol/m^2/s. Aqueous Fe(II) oxidation rates were calculated after Morgan and Lahav[38] at 20.5°C using a fixed total aqueous Fe concentration of 2.28e^{-4} mol/L. The pyrite dissolution and aqueous Fe(II) oxidation rates are in units of mol/m^2 mineral/s and s^{-1} (*), respectively. The pH range encountered by the carbonate-poor and carbonate-rich shales are indicated by pink-and green-shaded regions, respectively.

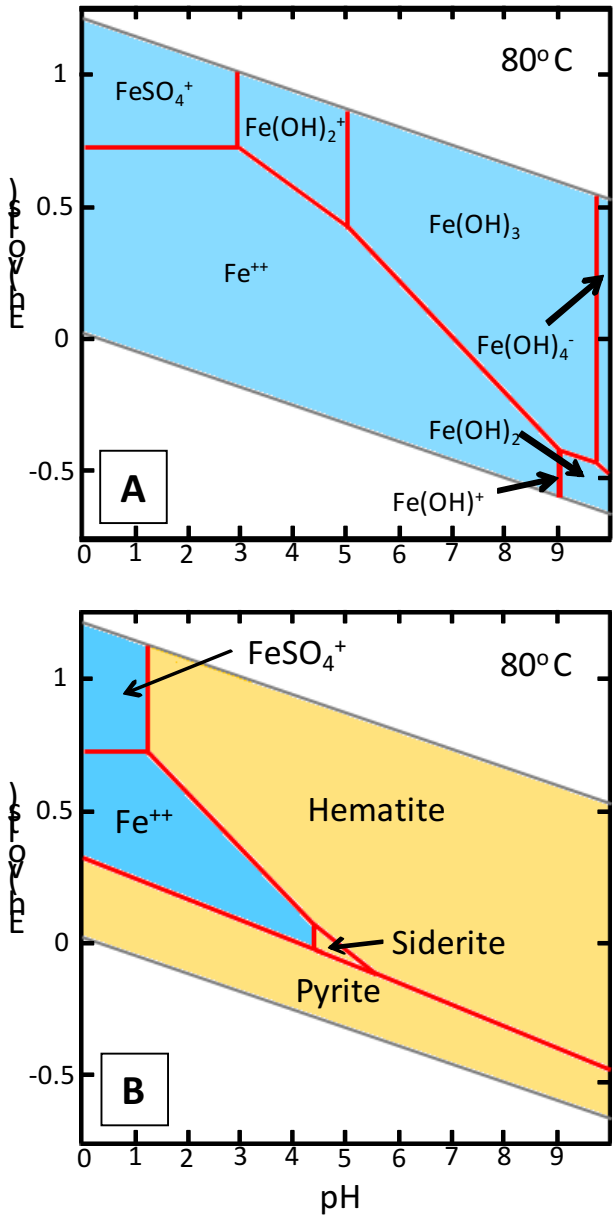

Figure 12: Eh/pH diagram for the Marcellus shale reactors (Blue denotes aqueous species while Orange denotes solid species). (A) Diagram of Fe aqueous species, all minerals suppressed. (B) Diagram of Fe species with no minerals suppressed showing that hematite is the predominant Fe(III)-bearing species at equilibrium. Diagram parameters: Fe = 4.66 x 10^{-4} M, Ca = 5.6 x 10^{-3} M, Mg = 4.94 x 10^{-4} M, HCO_3^- = 5.6 x 10^{-3} M, and SO_4^{2-} = 1 x 10^{-3} M.

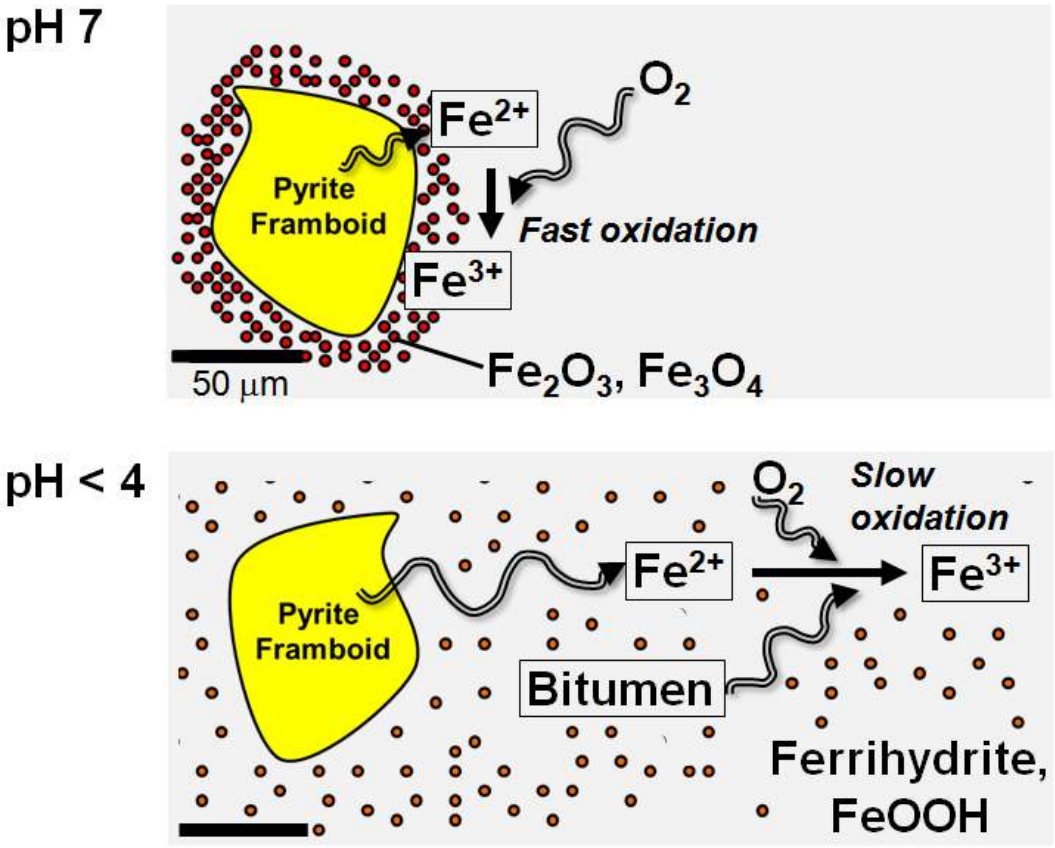

Figure 13: Conceptual model of Fe behavior in hydraulic fracturing systems based on solution pH. The pH 7 scenario occurs in systems with high carbonate concentrations or distances far away from the drill bore where injected HCl is neutralized (high carbonate) or very dilute (away from drill bore). The pH < 4 scenario is for low carbonate systems or near drill bores where the low pH slows down Fe(II) oxidation.